Investigation of Aerosol Particles Produced from Rapid Failure of Concrete

A thesis submitted to the University of Colorado Boulder
Department of Civil, Environmental, and Architectural Engineering
in partial fulfillment of the requirement for the degree of Master of Science

Eric W. Heichelheim
Candidate for M.S. Civil Engineering & B.S. Architectural Engineering

This thesis entitled:

"Investigation of Aerosol Particles Produced from Rapid Failure of Concrete"

written by Eric Heichelheim, under the supervision of Mija Hubler,

has been approved for the Department of Civil, Environmental, and Architectural Engineering.

Dr. Mija Hubler, Committee Chair

Dr. Yunping Xi, Committee Member

Dr. Jeong-Hoon Song, Committee Member

Date_____

The final copy of this thesis has been examined by the signatories, and we find that both the content and the form meet acceptable presentation standards of scholarly work in the above mentioned discipline.

ABSTRACT

Heichelheim, Eric W. (M.S., Civil Engineering, Department of Civil, Environmental, and Architectural Engineering)

Investigation of Aerosol Particles from Rapid Failure of Concrete

Thesis directed by Associate Professor Mija H. Hubler

This work addresses the hypothesis that modern concrete admixtures and inclusions have changed the microstructure mechanical properties sufficiently to result in undocumented concrete response to dynamic loading. The macro-, micro-, and nano- scale fragmentation of concrete as a function of different admixtures and inclusions is studied. This was done by loading them rapidly in a materials testing machine, with air sampling equipment standing by to sample the air, and collect the dust that resulted from the impact event. Four mixes were studied: regular Portland cement concrete for comparison, fly ash and slag admixtures to study effects of micro-scale inclusions, and steel-fiber reinforced concrete to study effects of macro-scale inclusions. Previous studies have shown that concrete fragments follow the Rosin-Rammler distribution as predicted by brittle fracture probabilities. This work concludes that such information is not representative of the aerosol particles that are generated, which are of primary importance for health. It is found that in particular the inclusion of large fibers generates a higher concentration of nanoscale fragments than the other admixtures. An improved analytical formulation for the probability of formulation of small fragments is developed.

ACKNOWLEDGEMENTS

Nicholas Cargill, B.S., Architectural Engineering, University of Colorado, Boulder, Colorado

Masters Student, University of Colorado Boulder

Role: Assistant

Lupita Montoya, Ph.D., Environmental Engineering, Stanford University, Stanford, California

Assistant Professor of Air Quality, University of Colorado Boulder

Role: Air Quality Consultant

Wyatt Champion, B.S., Environmental Engineering, University of Central Florida, Orlando, Florida

Research Assistant, University of Colorado

Role: Air Sampling Consultant

Jared Brown, Ph.D., Toxicology, University of Montana, Missoula, Montana

Associate Professor of Toxicology, University of Colorado Denver

Role: Nanotoxicology Consultant

Derek Carpenter, B.S., Mechanical Engineering, Missouri University of Science and Technology, Rolla, Missouri

Structures Lab Manager, University of Colorado Boulder

Role: MTS Consultant

Tim Porcelli, B.S. Candidate, Chemistry, University of Colorado, Boulder, Colo.

Undergraduate Researcher, Colorado Nanofabrication Laboratory, University of Colorado

Role: SEM Consultant

Brooke Smartz, LEED AP

Senior Market Manager, Sustainable Products, Holcim Inc.

Role: Slag Consultant

David Neel

Manager, Northwest Region, Boral Material Technologies LLC

Role: Fly Ash Consultant

Chuck Wilson

North America Distribution Manager – Technical Sales, Helix Steel

Role: Helix Consultant

Other Acknowledgements:

Harish Gadde**,** Shahlaa Al Wekeel**,** Adam Heichelheim, CU Boulder Innovative Seed Grant

CONTENTS

TABLE OF TABLES

TABLE OF FIGURES

1 INTRODUCTION

1.1 Purpose

The purpose of this thesis is to extend understanding of rapid microfracture in concrete, and the particles that are produced from such failure. Due to the scale of microfracture, these particles are prone to becoming airborne, creating aerosol particles. This thesis focuses on the effects of certain admixtures on the quantity, shape, and size of these particles. Prior developments in the field of concrete fracture mechanics are referenced and used to quantify the mechanical response these mixes exhibit under rapid compressive load.

When concrete structures are destroyed through extreme loading conditions, whether artificial or natural, a secondary risk to human health is imposed on top of the immediate and primary risk of collapse. Once the structural integrity has been compromised and the concrete has reached a crushing failure state, lung health is a concern for people near the collapsed structure. Concrete dust has been linked to lung complications, one group of such documented cases includes the first responders to the collapse of the World Trade Center in 2001[1] [2].

1.2 Goal

The goal of this thesis is to uncover how modern inclusions in concrete can affect the microstructure of the mortar. After conducting experimental work on specimens of concrete with different inclusions, theory that is well-established is applied to explain the mechanics of fragmentation, which is ultimately what produces the aerosol particles.

The overarching question in this thesis is whether there is an increased likelihood of negative long-term health effects from airborne particles produced from certain concrete mixes.

[1] Landrigan, et al, 731
[2] McGee, et al, 972

To answer this, the following questions pertaining to structural mechanics must be addressed in this thesis:

(a) How do inclusions to the mixture such as slag, fly ash, and steel fiber reinforcement, affect the concentration of airborne particles during failure?

(b) What particle characteristics, such as size distribution, shape, and quantity result from these inclusions?

(c) Is there a difference in mechanism between particle production with macro-scale inclusions, such as steel fiber reinforcement, and micro-scale inclusions, such as fly ash and slag?

It is predicted that mixes with small inclusions, such as fly ash and slag, will produce more particles per sample, and thus result in higher concentrations of dust in the air. It is also predicted that concrete particles in general will likely be harmful to lung health due to the shape of the particle. The background that helps arrive to this hypothesis is laid out in the Section 2.

1.3 Approach

The experimental work consists of making cylindrical test specimens of representative concrete mixtures with small inclusions like fly ash and slag, and large inclusions like steel fiber reinforcement, and compressively loading them in a materials testing machine at a rapid rate that simulates a member failure during a catastrophic loading event on a concrete structure. This loading is done in aerodynamic isolation, with air sampling equipment near the failed specimen. The air sampling equipment yields a real-time estimate of the concentration of dust in the air, but more importantly, samples actual particles that resulted from the loading event onto filters, for collection and further sizing, and medical studies. These results are combined with load data

recorded by the materials testing machine to analyze how certain admixtures affect the quantity, shape, and size distribution of particles produced from the concrete they constitute.

The characteristics of the fracture behavior of these mixes under rapid loading gathered from experimental data are then compared to theoretical predictions of these characteristics. One of these comparisons takes a prediction of fracture energy using comminution theory and compares it to the linear elastic fracture energy, given by an integral of the load-displacement data. Another comparison takes one of the bases of fragmentation theory and compares it to the empirical data gathered in this thesis. This fragmentation theory is then expanded to account for inclusions that cause stress concentrations.

2 BACKGROUND

2.1 Medical Background

This research does not study the link between airborne concrete dust and lung health, but it is motivated by this concern, and aids a research group at the University of Colorado Anchutz Medical Campus (headed by Dr. Jared Brown) who is studying this link. Two of the criteria for particles to be considered harmful to lung tissue are the shape and size of the particle. Shape is characterized by the shape factor, or aspect ratio, of a particle, defined by its average length over its average width, simplifying any particle to a cylinder with a height of the average length, and a diameter of the average width (See Figure 1a). The higher this ratio, the more elongated the particle, and the more likely it is to lodge itself into lung tissue and cause inflammation. This has been shown to occur with the inhalation of asbestos fibers[3]. Fibers are a classification of particle considered to exhibit this tendency, which the World Health Organization defines as having an

[3] Cooke, 147

aspect ratio of at least 1:3[4], or a shape factor of 3. Size is defined by the average dimension of a particle, simplifying it to a sphere with a diameter of that average dimension (See Figure 1b). Particles with an aerodynamic diameter greater than half a micron are considered both capable of becoming airborne, and able to easily interact with lung tissue once inhaled[5].

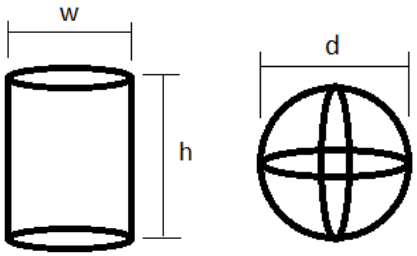

Figure 1a *Figure 1b*

Each aerosol particle can be simplified in shape to a cylinder with two average dimensions (1a), and in size to one average dimension (1b).

2.2 Air Quality Background

The most efficient way of determining the health risk of airborne contaminants is their concentration in the air. Environmental standards dictate which values of contaminant concentration are considered "dirty" and "clean." For PM10 particles (ten microns and under), the USA National Ambient Air Quality Standard puts the acceptable limit at 150 micrograms-per-cubic-meter, and the EC/UK Air Quality Standard puts it at 50 micrograms-per-cubic-meter[6]. In a "dirty" environment, one is more likely to inhale more airborne contaminant. In this case, the contaminant is microscopic fractured particles of concrete.

[4] Oberdörster, et al, 827
[5] Hering, 280
[6] Thompson, Visser, 111

2.3 Structural Mechanics Background

In order to study concrete particle formations from microfracture patterns, an understanding of concrete chemistry is required. Knowing the solidification of a concrete mix comes from the hydration reaction in its cement, attention to this chemical process can explain the structural behavior of the mortar. The hydration process consists of precipitation of calcium-silicate hydrates (C-S-H) onto all available surfaces. Initially, this precipitation forms layers of a microstructure (See Figure 2b)[7][8] that are very orderly, through a dynamic process, and the heat of hydration increases with time (See Figure 2a). However, once the space in between surfaces begins to fill up by these orderly layers of precipitate, the heat of hydration of the reaction decreases, and becomes a thermodynamic process (See Figure 2a)[9]. At this point, the hydration can only occur via diffusion in favorable locations through the pores, forming an irregular surface of the precipitate, and a more disorderly microstructure (See Figure 2b)[10].

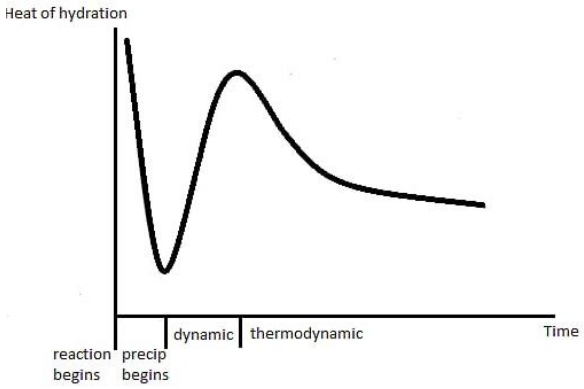

Figure 2a

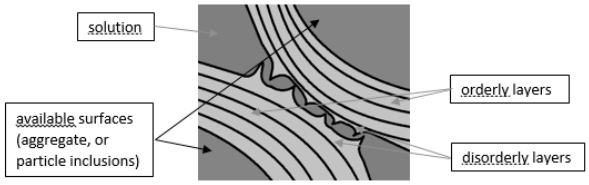

Figure2b

The heat of hydration for concrete has three phases, initial reaction, dynamic precipitation,and thermodynamic precipitation (2a). This is physically explained by precipitation filling the spaces between aggregate in the cement solution (2b).

[7] Kosmatka, Wilson, 59
[8] Neville, 36
[9] Neville, 16
[10] Neville, 17

The faster the rate of hydration, the quicker the dynamic precipitation can occur, forming a denser microstructure. In this case, these dense orderly layers tend to be less flexible, and thus more brittle, because of their ability to redistribute load through their close-knit network of chemical bonds. The thermodynamic precipitation tends to be stiffer as well, meaning all precipitation, which becomes the mortar of the concrete once the reaction dies out, is brittle[11]. This leads to a tendency to shatter into microscopic pieces under impulsive loading.

2.4 Hypothesis

The hypothesis is that the concrete with inclusions produces more airborne particles per specimen, and that these particles tend to be harmful to lung health. In order for this hypothesis to be plausible, several criteria need to be met:

(a) Microscopic concrete particles produced from microfracture must be small enough to become airborne and interact with human lung tissue.
(b) These particles must be elongated enough to be prone to lodging in lung tissue or cause inflammation.
(c) There must be large enough concentrations of these particles in the air in order for there to be an increased likelihood of inhalation of these particles.
(d) The mix itself must be brittle enough to be capable of producing such particles.

Due to the added surface area that additives like fly ash and slag provide, these substances tend to accelerate the hydration reaction, meaning a more brittle mortar due to reasons stated in Section 2.3. This leads to the hypothesis that these mixes are more likely to produce more harmful particles, as defined in Section 2.1, because the size produced is probably ideal for respiratory interaction, and also because these particles are probably elongated, as it has

[11] Neville, 414

been shown that stiffer concrete tends to produce more elongated particles at the smaller scale when crushed[12].

2.5 Related Studies

There have been several studies that research similar aspects of concrete fracture and comminution of concrete in structures. Some of these include "Simulation of high velocity concrete fragmentation using SPH/MLSPH" (Rabczuk, et. al., 2003[13]), "Dynamic fragmentation of concrete using electric discharge impulses" (Uenishi, et. al., 2014[14]), and "Dynamic fragmentation in concrete under impact and spalling tests" (Forquin, et. al. 2009[15]). However, two papers are most relevant to this thesis:

(a) "The fragmentation of standard concrete cylinders under compression: the role of secondary fracture debris" (Momber, 2000[16])

(b) "What Did and Did Not Cause Collapse of World Trade Center Twin Towers in New York?" (Bažant, et. al., 2008[17])

The first paper involved the same crushing procedure of concrete samples via a materials testing machine, however, particle collection consisted only of settled dust, mostly macro-scale dust particles that could not become airborne. The paper concluded that comminuted specimens of concrete produce debris with a size distribution that closely follows the Roslin-Rammler-Sperling-(Bennet) (RRSB) grain size distribution[16], and showed that the stiffer the concrete, the more elongated the smaller fracture debris particles tends to be[12].

---

[12] Momber, 454
[13] Rabczuk, et al
[14] Uenishi, et al
[15] Forquin, et al
[16] Momber, 452

The second paper, which investigates the energy embodied in the collapse of the World Trade Center in 2001, holds a section about the concrete decks in the World Trade Center, and studies the comminution of these decks during the collapse of each tower. From examining the particle sizes of the concrete debris after the collapse, which ranged from 0.01 mm to 0.1 mm, the concrete comminution energy computed for an initial particle size of 0.1 mm, and a resulting particle size of 0.01 mm, was in line with the kinetic energy produced from the gravitational effects of the collapse[17]. This thesis uses the same method for determining comminution energy in concrete. The method used matches the method outlined in Section 2.6.2.

2.6 Theory

2.6.1 Liner Elastic Fracture Mechanics

Linear elastic fracture mechanics (LEFM), proposes a way to predict fracture stress and crack propagation. A. A. Griffith[18] first proposed that the fracture stress, σ_f, is proportional to the square root of the surface energy of a pre-existing crack, as seen in Equation 1.

$$\sigma_f = \sqrt{\frac{EG}{\pi a}}$$

Equation 1[18]

Where E is the Young's modulus of the material, G is the fracture energy, and a is the crack length. If the applied stress exceeds this value, fracture occurs at the crack tip.

A different failure criterion was proposed by G. R. Irwin[19], which is a stress intensity factor, K, given by Equation 2.

[17] Bažant, et al, 900, 905
[18] Griffith, 176
[19] Irwin, 364

$$K_m = \sigma_m \sqrt{\pi a}\, f(\theta)$$

Equation 2[19]

Where m denotes which mode of fracture, σ_m is the applied stress in that mode, a is the crack length, and $f(\theta)$ is a function of the geometry and loading. If this quantity exceeds the fracture toughness of the material, cracking occurs where that factor has been exceeded.

The stress intensity factor is readily related to the energy release rate of the fracture, G, through Equation 3[20].

$$G_I = \begin{Bmatrix} {K_I}^2 \left(\frac{1-\nu^2}{E}\right) \; plane\ strain \\ \frac{{K_I}^2}{E} \; plane\ stress \end{Bmatrix} \; G_{II} = \begin{Bmatrix} {K_{II}}^2 \left(\frac{1-\nu^2}{E}\right) \; plane\ strain \\ \frac{{K_{II}}^2}{E} \; plane\ stress \end{Bmatrix} \; G_{III} = \frac{{K_{III}}^2}{2\mu}$$

$$G = G_I + G_{II} + G_{III}$$

Equation 3[20]

Where the subscript numerals denote which mode of fracture, K is the stress intensity factor given by Equation 2, ν is the Poisson's ratio of the material, E is the Young's modulus of the material, and μ is the shear modulus of the material.

The energy going into a material under loading is defined by the area under the loading curve, which represents force over displacement. In a classical physical sense, it is the work done externally to the system. According to LEFM, the total fracture energy is equal to this external work, minus the complimentary energy, represented by the area under the triangle connecting the origin to the point of fracture on the loading curve (See Figure 3)[21].

[20] Martel, 9
[21] Bazant, Planas, 30

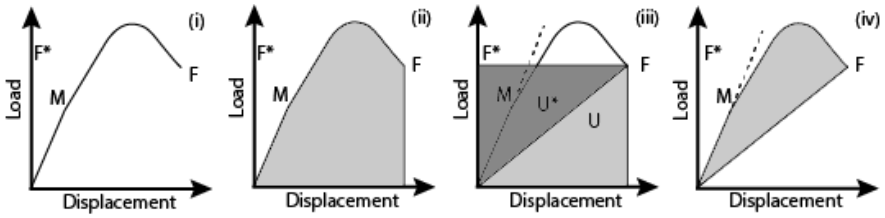

Figure 3[21]

The fracture energy according to LEFM theory is found from the load curve (i), by integrating underneath it (ii), and subtracting the complimentary energy, U (iii), and is thus represented by the area shown in (iv).

This is because of the assumption that the energy is internally stored in elastic strain, and is accurate to within 2%, so long as the size of aggregate is below a certain limit. For compression, this limit is given by Equation 4[22].

$$D \geq 46 d_a$$

Equation 4[22]

Where D is the depth of the specimen, and d_a is the maximum aggregate size. For eight-inch-deep cylinders, the maximum aggregate size for this condition is about 0.2 inches. Beyond this, the size effect distorts the prediction of fracture energy. As shown in Section 3.2, nearly all specimens do not meet this limit, so this prediction of fracture energy is off by a certain amount. As seen in Figure 4[23], this error can be predicted because the exceedance of this limit is known.

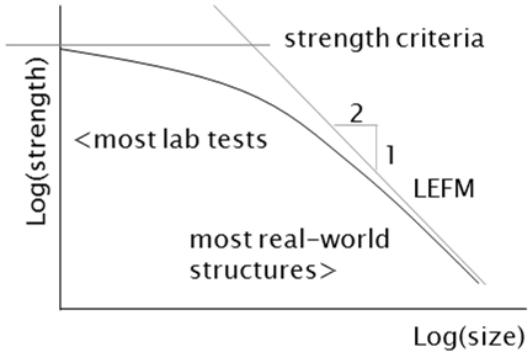

Figure 4[23]

The size effect distorts concrete strength, and therefore other properties, due to the multiple length scales of its components.

[22] Bazant, Planas, 111
[23] Bazant, Planas, 9

2.6.2 Comminution

Comminution theory focuses on quantifying the phenomenon of a material crushing into smaller pieces. It stems from a mining engineering practice called comminution where ore is crushed into finer particles. The original theory behind the design of the machines that would do this comes from Equation 5[24], in which the energy to produce these smaller particles can be found through integration of this differential relation.

$$dE = -C\frac{dx}{x^n}$$

Equation 5[24]

Where C is a multiplier dependent on the material being crushed, x is the size of particle, dx is the size differential in a grain size distribution, and dE is the differential energy required to crush a particle of size x into a size smaller by dx. n is a parameter for integration along the grain size distribution. If n = 1, the relation is suitable for large particles, and becomes Kick's Law, given by Equation 6[24].

$$E = C\log\frac{x_1}{x_2}$$

Equation 6[24]

Where the subscripts 1 and 2 denote before crushing and after crushing, respectively. When n = 2, the relation becomes a proposal by Peter von Rittinger, suitable for relatively small particles, given by Equation 7[24].

$$E = C\left(\frac{1}{x_2} - \frac{1}{x_1}\right)$$

Equation 7[24]

[24] Tanaka, 353

Fred Chester Bond formulated a compromise between these relations. His law is equivalent to holding *n* between one and two, and yields Equation 8[24].

$$E = W_i\left(\frac{R^r - 1}{R^r}\right)\left(\frac{100}{x_2}\right)^r$$

Equation 8[24]

Where R is the size reduction ratio equal to x_1/x_2, r is the deviation from Kick's law, equal to $n - 1$, and W_i is the Bond work index, which is dependent on the material being crushed. For cement in concrete, the Bond work index could be close to limestone ore: 10-20 kilowatt-hours per short-ton[25]. By setting r equal to ½, Bond's exponent *n* becomes 1 ½, which Bond explained was representative of the strain energy initially being proportional to the volume of the sample being crushed, and then transferring into crack energy proportional to the crack surface area[24]. Due to a good representation of most materials at all sizes[25], an r of ½ is used in this thesis, meaning after some treatment, the comminution energy becomes that given by Equation 9[25].

$$E = 10W_i\left[\frac{1}{\sqrt{x_2}} - \frac{1}{\sqrt{x_1}}\right]$$

Equation 9[25]

Whose units are kilowatt-hours per short ton, given the quantities $\frac{10}{\sqrt{x_1}}$ and $\frac{10}{\sqrt{x_2}}$ have units $\frac{\sqrt{\mu m}}{\sqrt{\mu m}}$[25].

2.6.3 Fragmentation

Similar to comminution, this theory predicts a size distribution curve for fragments produced from single brittle fracture in an infinite domain due to a random and independent distribution of Griffith flaws[26]. This theory assumes the nucleation of cracks occurs at random flaws, and the nucleated cracks propagate towards one another in order to form these fragments. However, it is important to note the limitations of this theory, as it further assumes a

[25] The Visual Computer
[26] Gilvarry, 393

homogeneous material with no viscoelastic or plastic effects, which does not match the properties of concrete. Despite this, the theory can be used as a point of reference for the experimental results.

The sizes of these fragments are explained by one formulation for a fragmentation theory by J.J. Gilvarry. Beginning with an infinite three-dimensional domain with Griffith-type flaws, which form brittle fracture when activated, is analogous to the interior of a concrete specimen that is assumed to be brittle. These flaws are assumed to be distributed randomly and independently in a Poisson distribution, so the probability that n flaws exists in a sub-domain t is given by Equation 10[27].

$$P(n|t) = \frac{e^{-\gamma t}(\gamma t)^n}{n!}$$

Equation 10[27]

Where γ is the mean density of flaws in the infinite domain. If the sub-domain were to be a potential fragment, then this relation can be used to relate fragment size to flaw spacing. Gilvarry selected a sub-domain represented by a three-dimensional geometry with three fracture surfaces, *s*, intersecting each other to form a volume, *v*, with three edges of equal length, *l*[28] (See Figure 5). The differential geometry used for integration is similar (See Figure 5).

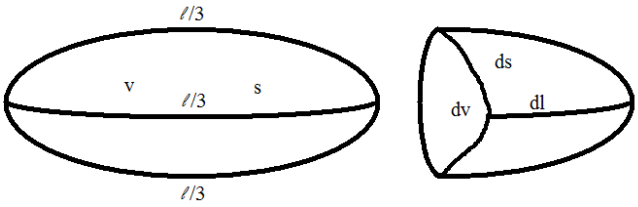

Figure 5

The Gilvarry fragment is a mathematical volumetric domain representing a piece of material resulting from single brittle fracture, in which probabilities of finding Poisson-distributed flaws can be defined as 0 within the fragment, and 1 on the edges or surface of the fragment.

[27] Gilvarry, 393
[28] Gilvarry, 394

The definition of this fragment according to Gilvarry dictates that there must be at least one flaw on the edge, surface, or in the volume of the fragment, and no flaws leftover in the volume of the fragment[28]. This is embodied in Equation 11.

$$dp(l,s,v) = P(0|l,s,v)P(1|dl,ds,dv) = P(0|l)P(0|s)P(0|v)[P(1|dl) + P(1|ds) + P(1|dv)]$$

Equation 11[28]

Substituting Poisson's distribution and simplifying, this expression for differential probability is given by Equation 12.

$$dp(l,s,v) = e^{-Q}dQ, \qquad Q = \gamma_l l + \gamma_s s + \gamma_v v$$

Equation 12[28]

Integrating *dp* thrice among *l*, *s*, and *v*, and applying unity of mass, yields the predicted distribution: the percent smaller than a certain size described by *l*, *s*, and *v*, and in turn *Q*. If all the fragments are assumed to be similar in shape, which could be the case under uniaxial compression, the expression becomes dependent on the distribution of the *l*-*s*-*v* flaws[29].

$$Y(Q) = 1 - e^{-Q}, \qquad Q = \gamma_l l + \gamma_s s + \gamma_v v \rightarrow Q = \frac{x}{k} + \left(\frac{x}{j}\right)^2 + \left(\frac{x}{i}\right)^3 \ for\ similar\ shapes$$

Equation 13[29]

Furthermore, for small sizes, the "*l*" flaws, or edge flaws, dominate, yielding Equation 14[30].

$$Y(x) = 1 - e^{\frac{x}{k}}$$

Equation 14[30]

Where *k* is physically the mean spacing of the edge flaws in the original domain. (*i* and *j* are similar parameters.) Interestingly, this is the first-order Rosin-Rammler (or RRSB) grain size

[29] Gilvarry, 396
[30] Gilvarry, 397

distribution, which was found for the finer dust of concrete in Momber's study, as summarized in Section 2.5.

3 EXPERIMENTS

3.1 Procedure

The procedure followed for testing can be found in Appendix I: Procedure for Production and Collection of Airborne Comminuted Concrete Particles. The purpose of the tests is to replicate an extreme loading event that would produce airborne dust from the concrete as it is crushed. The concentration of dust is measured, and the dust is sampled, so that it can be analyzed for toxicity, as well as shape and size statistics. Load-displacement data is recorded and analyzed, along with the mass and concentration of dust produced.

3.2 Materials

Four mixes are prepared, broken, sampled, and imaged for this thesis. For comparison one was a standard Portland cement concrete mix, while two other mixes contained replacement fly ash or slag, and the last mix included macro-scale inclusion of steel fiber-reinforcement. The fly ash and slag exemplify the smaller inclusions that are predicted to cause higher concentrations of dust in the air. The wire reinforcement is tested on behalf of Helix, but also aids this thesis as a counterexample to the smaller inclusions. Details of the mixes are shown in Table 1.

Table 1: Details of Concrete Mixes Tested

Mix	Cylinders Poured	Max. Size Aggregate	Cement Content	Gravel Content	Sand Content	Water Content	Inclusion Content	Inclusion to Cement Ratio	Fiber-Reinf. Dosage
Regular	33	0.75"	15.1%	45.3%	30.2%	9.4%	-	-	-
Slag	30	0.75"	12.0%	43.0%	32.0%	9.0%	4.0%	1:3	-
Fly Ash	30	0.75"	12.0%	43.0%	32.0%	9.0%	4.0%	1:3	-
Helix 1-3	3	0.2"	12.4%	44.4%	33.1%	9.3%	0.8%	-	31 lb/cy
Helix 4-10	7	0.5"	12.4%	44.4%	33.1%	9.3%	0.8%	-	31 lb/cy

Cement is Quikrete® Type I/II Portland Cement, and meets ASTM C-150[31].The average Blaine fineness for Type I in accordance with ASTM C-150 is 384 m^2/kg, while that for Type II is 377 m^2/kg[32]. For the chemical composition of Portland cement, see Table 2.

Figure 6a

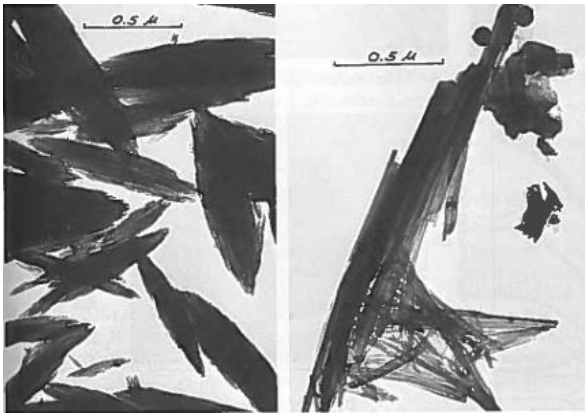

Figure 6b [28]

Type I/II Portland Cement, a photograph (6a) and an SEM image (6b).

Table 2: Chemical Composition of Typical ASTM C-150 Type I/II Portland Cement [29]

Clinker Phase Compound	**Average Composition in Type I Portland Cement (ASTM C-150)**	**Average Composition in Type II Portland Cement (ASTM C-150)**
C_3S	57%	57%
C_2S	15%	17%
C_3A	9%	7%
C_4AF	8%	10%
Product Compound	**Average Composition in Type I Portland Cement (ASTM C-150)**	**Average Composition in Type II Portland Cement (ASTM C-150)**
SiO_2	20.2%	20.9%
Al_2O_3	5.1%	4.6%
Fe_2O_3	2.7%	3.3%
CaO	63.2%	63.7%
MgO	2.5%	2.0%
SO_3	3.3%	2.9%
Na_2O	0.7%	0.56%

[31] ASTM International
[32] Kosmatka, et al, 51

For completeness, shown here are the primary hydration reactions [33]:

$$2(3CaO \cdot SiO_2) + 11H_2O \xrightarrow{yields} 3CaO \cdot 2SiO_2 \cdot 8H_2O + 3(CaO \cdot H_2O)$$

$$Tricalcium\ silicate\ +\ Water \xrightarrow{yields} Calcium\ silicate\ hydrate\ +\ Calcium\ hydroxide$$

$$2(2CaO \cdot SiO_2) + 9H_2O \xrightarrow{yields} 3CaO \cdot 2SiO_2 \cdot 8H_2O + CaO \cdot H_2O$$

$$Dicalcium\ silicate\ +\ Water \xrightarrow{yields} Calcium\ silicate\ hydrate\ +\ Calcium\ hydroxide$$

$$3CaO \cdot Al_2O_3 + 3(CaO \cdot SO_3 \cdot 2H_2O) \xrightarrow{yields} 26H_2O + 6CaO \cdot Al_2O_3 \cdot 3SO_3 \cdot 32H_2O$$

$$Tricalcium\ aluminate\ +\ Gypsum \xrightarrow{yields} Water\ +\ Ettringite$$

$$2(3CaO \cdot Al_2O_3) + 6CaO \cdot Al_2O_3 \cdot 3SO_3 \cdot 32H_2O \xrightarrow{yields} 4H_2O + 3(4CaO \cdot Al_2O_3 \cdot SO_3 \cdot 12H_2O)$$

$$Tricalcium\ aluminate\ +\ Ettringite \xrightarrow{yields} Water\ +\ Calcium\ monosulfoaluminate$$

$$3CaO \cdot Al_2O_3 + CaO \cdot H_2O \xrightarrow{yields} 12H_2O + 4CaO \cdot Al_2O_3 \cdot 13H_2O$$

$$Tricalcium\ aluminate + Calcuim\ hydroxide \xrightarrow{yields} Water\ +\ Tetracalcium\ aluminate\ hydrate$$

$$4CaO \cdot Al_2O_3 \cdot Fe_2O_3 + 10H_2O \xrightarrow{yields} 2(CaO \cdot H_2O) + 6CaO \cdot Al_2O_3 \cdot Fe_2O_3 \cdot 12H_2O$$

$$Tricalcium\ aluminate\ +\ Water \xrightarrow{yields} Calcium\ hydroxide\ +\ Calcium\ aluminoferrite\ hydrate$$

Fine aggregate is provided in the form of Quikrete® All-Purpose Sand, which is washed, properly graded, and meets ASTM C-33[34]. The grain size distribution follows grading requirements laid out in Section 4, Table 1 of ASTM C-33[34] (See Appendix II: Further Information on Mix Components).

[33] Kosmatka, et al, 49
[34] ASTM International

Figure 7

Fine aggrgegate is provided in well-graded sand.

Course aggregate is provided in the form of Vigoro® Pea Pebbles and Quikrete® All-Purpose Gravel, which is washed, properly graded, and meets ASTM C-33[34]. The grain size distribution follows grading requirements laid out in Section 4, Table 3 of ASTM C-33[34] (See Appendix II: Further Information on Mix Components).

The maximum aggregate size was varied in order to vary the errors in fracture energy as predicted by LEFM theory, which is explained in Section 2.6.1. Commercial-grade concrete generally uses ¾" maximum-sized aggregate, so this was available in the Quikrete® gravel. Pea pebbles are smaller, and tend to be under about ½" maximum. The 0.2" is the maximum size for aggregate if the LEFM prediction for fracture energy is to be accurate within 2%. This was achieved through sieving, and was only done for three cylinders to quantify the theoretical error.

Figure 8a *Figure 8b* *Figure 8c*

Large aggregate is provided in ¾" gravel (8a), pea gravel (8b), and sieved 0.2" gravel (8c). The size is varied for different deviations from LEFM via the size effect.

Slag is granulated blast-furnace slag provided by Holcim, Inc. For the chemical composition of the slag used, see the attached analysis report provided by Holcim, Inc. The individual particles of slag are typically less than 45 microns, with a Blaine fineness of about 400 to 600 m^2/kg[35].

Figure 9a *Figure 9b[30]*

Granulated blast furnace slag, a photograph (9a) and an SEM image (9b).

Fly ash is Class C fly ash provided by Boral Material Technologies, LLC. It meets ASTM C618[36] and AASHTO M295[37]. For the chemical composition of the fly ash used, see the attached analysis report provided by Boral Material Technologies, LLC. The individual particles of fly ash typically range from less than 1 micron to more than 100 microns, with an average size of 10 microns[38].

Figure 10a *Figure 10b[31]*

Class C fly ash, a photograph (10a), and an SEM image (10b).

[35] Kosmatka, et al, 70
[36] ASTM International
[37] AASHTO
[38] Kosmatka, et al, 69

Macro-scale inclusions are steel fiber-reinforcement provided by Helix. They mix into concrete to provide reinforcement in slabs and walls in the absence of wire-reinforcement mesh or rebar. The steel fibers are very large compared to the slag and fly ash. They are wound wires, about 24-ga (0.02 inches), cut into 1 inch-long pieces.

Figure 11a *Figure 11b*

Steel fibers are cut steel wires twisted in a helical shape for bonding ability.

3.3 Equipment

The equipment used to crush the concrete specimens is an 810-model materials testing machine from MTS, housed by the University of Colorado Boulder structures laboratory. It uses two hydraulic pumps in order to produce high loads by the piston. With the platen attachments, the piston can apply a compressive load to test specimens. The top platen is a rotatable plate whose position is fixed by a crosshead that can be adjusted and locked on two rails (See Figure 12). The bottom platen is a non-rotatable plate attached to a piston controlled by hydraulic pressure. A computer controls the movement of the piston, and thus the loading rate on the specimen.

Figure 12

The setup for specimen crushing was a materials testing machine whose safety enclosure was sealed with painter's tarp and duct tapefro aerodynamic isolation.

The equipment used to sample and measure airborne dust is provided by a research group at the University of Colorado Boulder (headed by Dr. Luptia Montoya) who performs various air quality studies. Two types of machines are used for this thesis. One samples aerosol particles and collects them onto a filter, and the other optically tracks dust and predicts the concentration in real-time. The aerosol sampler used is the MiniVol™ from Airmetrics (See Figure 13a), and the optical aerosol tracker used is the DustTrak™ from TSI (See Figure 14a).

The MiniVol sampler, hereon referred to as "MiniVol," uses an air pump that draws air at any rate up to ten liters per second to capture particles in that air. The method used for this is impaction, a form of inertial collection which utilizes the aerodynamic resistance of the airborne particles in order to separate them by size [39]. This is carried out by a funnel that increases the velocity of the air, which is then pushed downward against a small flat surface that has been treated with oil (See Figure 13b). The airflow around this surface continues to a Teflon filter with a 2.0-micron mesh. The air flows through the mesh, leaving behind the airborne particles to be captured. The size of these particles is controlled by the aerodynamic interaction of the

[39] Hering, 280

particles and the oiled surface. The surface, known as the impactor plate, creates a positive pressure zone where particles of a certain aerodynamic diameter are theoretically too large escape. What are left behind are the smaller particles below the size cutoff that are physically able to continue to the filter, where they are collected. In order to observe the most particles possible, PM10 (ten microns and under) is set as the cut off for this thesis, which means given the aperture of the funnel, the airflow is set to 5 liters per minute in order to uphold the PM10 size cutoff[40]. Maintaining this flow to within ±10%[41] will accurately provide this cutoff to within ±2%[42], and has been shown to produce 50% collection efficiency as designed[43].

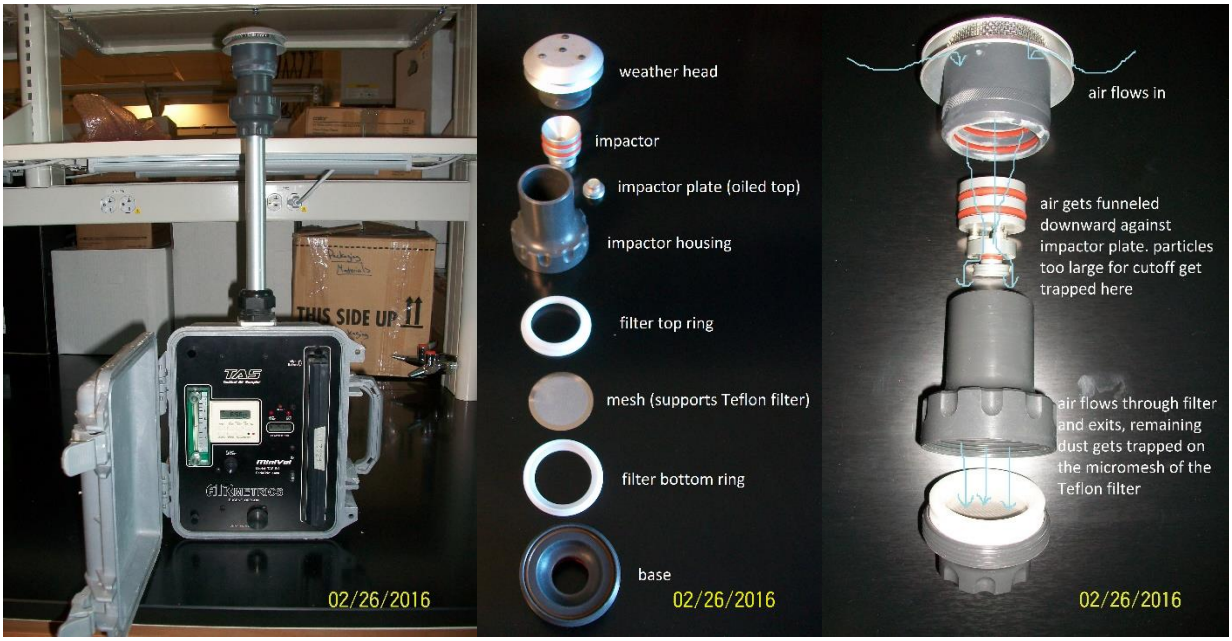

Figure 13a *Figure 13b* *Figure 13c*

The MiniVol (13a) samples air and captures airborne particles onto Teflon filters. The assembly (13b) is designed for the aerodynamic process of impaction (13c).

[40] Airmetrics, 28
[41] Airmetrics, 10
[42] Airmetrics, 17
[43] Hill, et al., 9

The DustTrak Aerosol Monitor, hereon referred to as “DustTrak,” uses a similar procedure for sampling air, but does not collect particles for this thesis. The air sample is pumped from an intake to a small chamber where a spectroscope detects light scattering off particles and estimates the concentration in real time. Due to the indirect nature of the optical tracking method, this machine is much less accurate than the MiniVol in predicting particle mass, but can capture a time-history which correlates to the loading profile.

Figure 14

The DustTrak also samples air, but uses light scattering to predict what concentration of particles is in the air it is sampling.

The equipment used to image the microscopic particles is a scanning electron microscope (SEM), housed by the Nanomaterials Characterization Facility at the University of Colorado Boulder. Using electron feedback from the radiation given off by a tungsten filament, images of the samples can be produced down to several microns. Samples being imaged are sputter-coated with gold, then secured on a stage and placed in a chamber that gets evacuated for the best clarity of electron feedback (See Figure 15).

Figure 15

The scanning electron microscope is used to analyze the Teflon filters after collection. This was done for fly ash and slag concrete samples only.

3.4 Medical Lab Tests

Used by Dr. Jared Brown and his team at Anchutz Medical Campus, the dust collected on the Teflon filters is removed by soaking the filters, and suspending the captured particles in solution through the process of sonication. Sonication uses sonic energy to agitate particles in solution, utilizing a pump and actuator that varies the pressure at ultrasonic vibration amplitudes. The solution used is a phosphate buffer saline (PBS).

Dynamic light scattering (DLS) is used to characterize the size of the particles at the micro- and nano- level. Using a laser and spectroscopy equipment, the particles undergo Rayleigh scattering when the light hits them, and the scattered reflected light is measured, which tells something about the scale of the particles.

Using dichloroflourescein, (DCF), and MitoSOX, a mitochondrial superoxide indicator, the particles can be tested for oxidative stress. In short, by interacting with test cells in the presence of these chemicals, the measure of this interaction with the particles can be recorded as the oxidation stress on the cell.

3.5 Setup

Unreinforced cylindrical specimens of diameter 3.94 in. (100 mm) and length 7.87 in. (200 mm) were cured for 28 days in a fog room. The concrete specimens must be broken in aerodynamic isolation in order to both contain the particles in a small space for collection, and minimize background particles from the surrounding environment. This was achieved by outfitting the safety enclosure around the materials testing machine with plastic painter's tarp and duct tape (See Figures 16a and 16b). In this chamber, the sampling equipment was placed strategically in the chamber, with a fan running in the corner in order to facilitate the movement of particles (see Figures 16c and 16b). One at a time, specimens were placed onto the bottom platen through the access door, and were crushed with the door closed and sealed. Based on preliminary measurements with the DustTrak, it was known that after a loading event, it takes on average about seven minutes for the concentration to decrease to 1% of the peak concentration caused immediately after failure. Therefore, a 10 minute collection time was ensured between loading events, in order to collect the most particles possible, and to isolate peaks in concentration to their respective specimens.

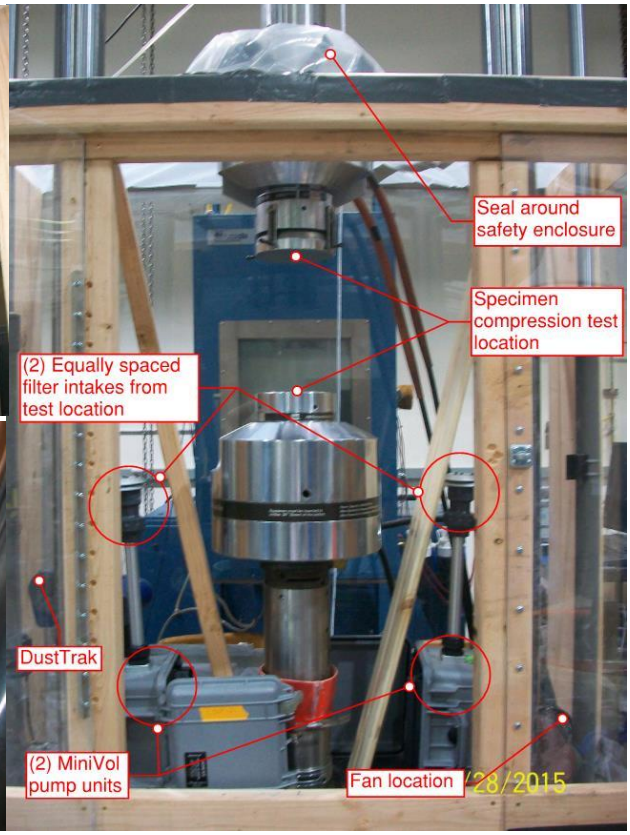

Figure 16a (Top) and Figure 16b (Bottom) *Figure 16c*

The setup for specimen crushing was a materials testing machine whose safety enclosure was sealed with painter's tarp and duct tape (16a) for aerodynamic isolation. A fan (16b) facilitated air movement, so that the sampling equipment (16c) could smaple the most particles possible.

4 RESULTS

Presented here are the data collected from the experimental testing, whose procedure is laid out in Appendix I: Procedure for Production and Collection of Airborne Comminuted Concrete Particles. Again, recorded are the:

(a) Load-displacement data recorded by the materials testing machine

(b) Real-time dust concentration data predicted by the DustTrak

(c) Average dust concentration predicted from mass collected onto the filters in the MiniVols

(d) Size and shape data measured on scanning electron micrographs by an image processor

4.1 Load-Displacement Data

These load curves were recorded by the MTS software controlling the load in the piston of the materials testing machine. Displacement of the piston was held constant with time, at a selected rate of 0.075 inches per second. This is consistent with what could be seen in a typical concrete beam during a violent earthquake (See Appendix IV: Calculations). The piston load, in kips, and piston displacement, in inches, are recorded every 0.01 seconds. Recording begins when loading begins, and recording ends when loading ends, which is right when failure occurs or begins to occur. It is important to note that loading is manually stopped, introducing a source of error in the data in terms of fracture energy. Furthermore, some of the specimens producing particles being examined for toxicity were capped with a standard sulfur compound, while some were capped with rubber encased in steel plates, due to a shortage of the sulfur compound. This difference in boundary conditions is reflected in the load curves of the two cases, as can be seen in the original complete data in Appendix III: Complete Data. To remedy this, more tests were run with the sulfur compound on the specimens that lacked it, and their curves are analyzed in place of the original curves. Post-processing of the data zeroed the beginning displacement and load and eliminated outlier specimens. For complete data, see Appendix III: Complete Data. See Figure 17 for the consistent load-displacement curves.

With regard to the aggregate size, what stood out was the wire-reinforced specimens containing the 0.2-inch gravel. As can be seen in Appendix III, these specimens were considerably weaker than the other wire-reinforced specimens. Given that theoretically, they are accurate enough to ignore the LEFM size effect, their energy must be more accurate than the others. Though this is useful information, these specimens are identified as outliers, and a theoretical error is recognized for the other wire-reinforced specimens, which have 0.5-inch

gravel, and all other specimens, which have 0.75-inch gravel. With an examination of these errors, it is concluded that the error for ½" pea gravel is about 20%, and that for ¾" gravel is about 27%. This is discussed further in Section 6.2.1, and the calculation that arrives to this is in Appendix IV: Calculations.

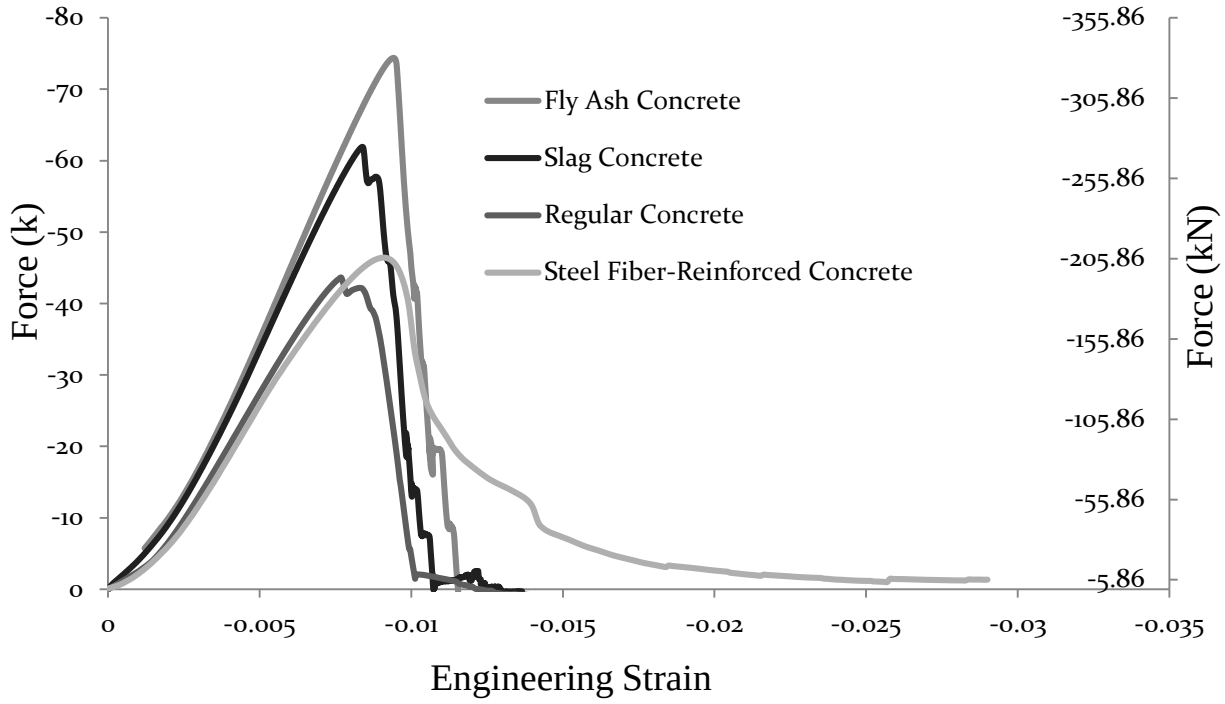

Figure 17

From the average consistent load-strain curves shown for each concrete tested, it is clear the fly ash and slag added stiffness and strength to their respective mixes. The Helix fibers added minimal strength and an neglibable effect on stiffness.

One observation that can be made is that the steel fiber reinforcement softened the failure compared to the more brittle failures by the other types. Also, the smaller inclusions evidently strengthened and stiffened the concrete. The external work on the specimens found from integrating these curves is very close to the linear elastic fracture energy, due to the fracture point being so close to zero load when recording stopped approximately at the advent of brittle

fragmentation. The lack of complimentary energy can be attributed to the rapid load, and the reason for its occurrence implies all the external work done by the compression is released in a sudden burst. See Section 4.5 for the computed average mechanical properties for each mix.

4.2 Real-Time Dust Concentration Data

These curves are a measure of dust concentration in the air over time, measured optically by the DustTrak with air sampled from its intake. Unfortunately, the data from the original tests was lost. Furthermore, the machine was broken during additional crushing. So shown here are the concentrations measured from initial tests (See Figure 18) where at the time, the only aerodynamic isolation was a tarp draped over a bare materials testing machine. This is not a critical setback, as this data is secondary, and more so acts as a proof of concept.

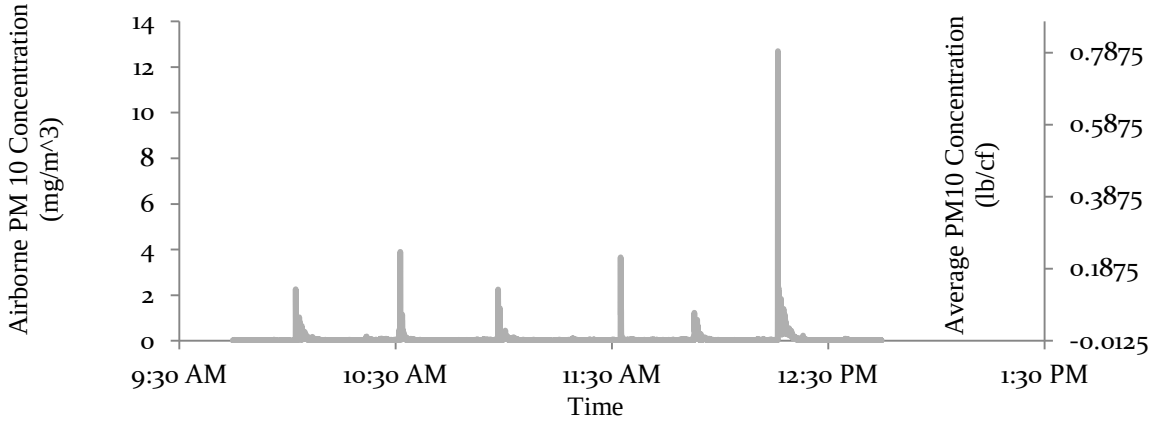

Figure 18

The data recorded by the DustTrak during preliminary tests shows estimated aerosol concentration over time. Each spike in dust concentration correlates to a crushing failure of the concrete specimens.

It can be seen here that clearly each loading event produces a spike in dust concentration, which does not die out for several minutes.

4.3 Dust Concentration Data from Mass Collected

The air the MiniVols sampled is assumed to be aerodynamically isolated by seals of the safety enclosure around the materials testing machine. However, error could have arisen through the opening of the door for specimen access, as well as unexpected holes in the painter's tarp created by falling shrapnel from the specimens. Diligence to tape these up was exercised, but the enclosure was never perfectly sealed.

Table 3 shows the concentration predicted from the mass collected onto each filter used. By taking the runtime of each session, the flow rate can be multiplied by this runtime to compute the total air moved through the MiniVol during the session, which can combine with the mass collected on each filter to predict the average concentration in the air during the session. With two for each concrete type, eight filters containing particles were weighed after sampling. Weighing these filters is a delicate procedure where a box around the scale is conditioned to have minimal air movement. The filters used are pre-weighed before any use, so that they can be subtracted from the weight after sampling for the weight of particles collected onto the filters. For the raw weight data, see Appendix III: Complete Data. For the final mass and concentration data, see Table 3.

Table 3: Average Concentrations Produced by each Concrete Tested

Concrete Type	**Run Time (hrs)**	**Filter A Mass (µg)**	**Filter B Mass (µg)**	**Mass per Specimen (ug)**	**Two-Sampler Average Airborne PM10 Concentration (µg/m^3)**
Regular	5.1	480	565	49.8	318
Slag	5.1	1300	1080	99.2	609
Fly Ash	5.5	1470	2075	142	865
Wire-Reinforced	1.1	15	70	8.50	64

It is observed that the mass collected per specimen ranks with the steel fiber-reinforced concrete at the least, then the regular concrete, then the slag concrete, then the fly ash concrete. It is more useful in environmental engineering if this is translated to a concentration. But even with the average concentration from two samplers, this trend still holds. Meaning that this experiment reveals that wire-reinforced concrete produces far less PM10 airborne particles than regular concrete, and slag and fly ash both produce more. See Figure 19 for a graphical representation of this, normalized with regular concrete.

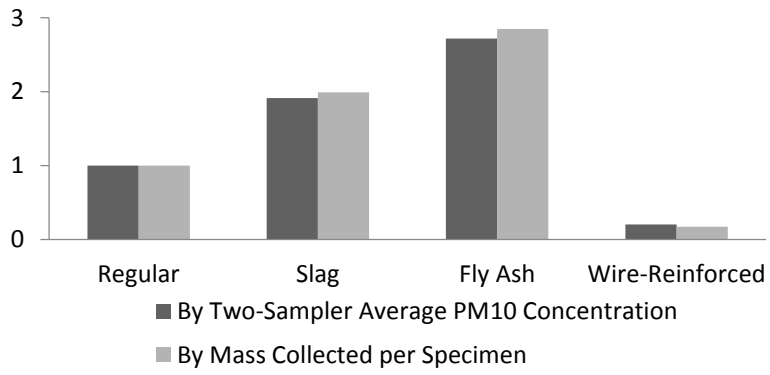

Figure 19

A normalized chart visually representing the particle production per concrete type shows the trend for aerosol production. The mass collected per specimen is compared against the average concentration, which takes runtime into account. Both measurements, though different, yield the same trend.

4.4 Particle Characteristics

When redoing the load curves for fly ash and slag concrete specimens that had missing capping compound, collection of airborne particles was repeated, but these samples underwent

SEM imaging. By observing the microns-large particles trapped in the filter, it is evident there is a tendency of elongation (See Figures 20a and 20b).

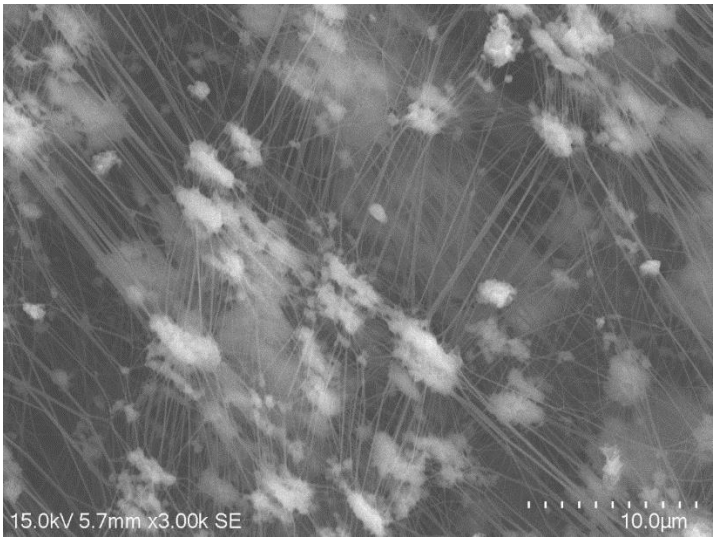

(Fly Ash Concrete)

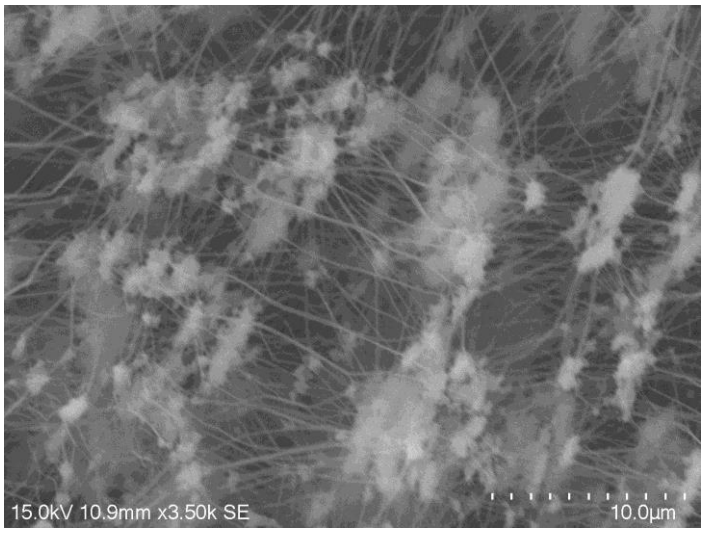

(Slag Concrete)

Figure 20a (Top), Figure 20b (Bottom)

These SEM images of some aerosol particles from fly ash concrete (20a) and slag (20b) entangled in the Teflon filter show that there is evidence of elongation in these particles, supporting the hypothesis that they can be harmful to lung health. However, a separate toxicity analysis is required to determine more confidently.

By inspection, it is clear that some of these particles show shape factors of at least 3, which is the threshold for lung health concerns as mentioned in Section 2.1. It is important to note that though this shape factor is a marker for inflammation, and ultimately toxicity, it does not reveal whether these particles can be harmful. A nanotoxicity and inflammation test in-vitro, and eventually in-vivo, will need to be performed to tell for sure if these particles are harmful. The particles collected in this thesis were not enough to make that conclusion from the test. Again, this thesis focuses on the mechanical aspect of these particles, as opposed to this aspect.

From a dynamic light scattering analysis performed at the Anchutz School of Pharmacy, under the University of Colorado Denver, the size distribution of the particles found through dynamic light scattering are presented here, in Figure 21.

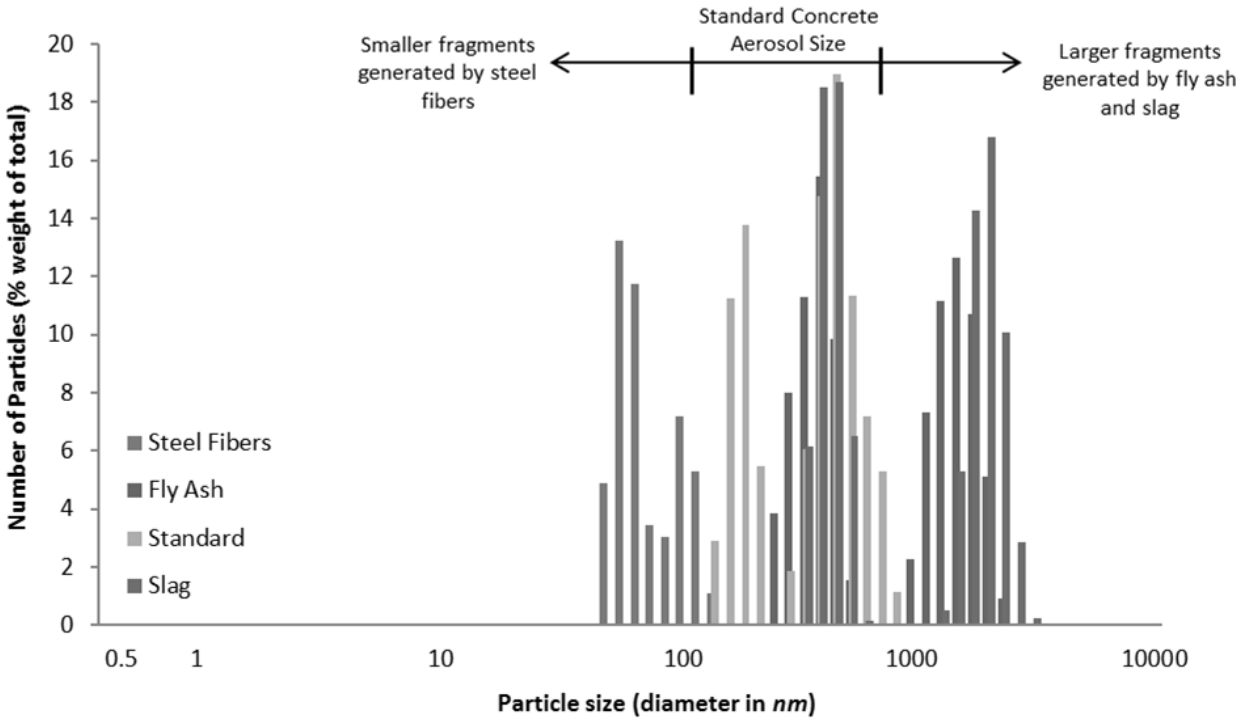

Figure 21

The size distributions of the aerosol particles sampled from the air, generated from each concrete type reveals that steel fiber-reinforced concrete produced much smaller aerosol particles than the other mixes.

The particles collected seem to exhibit a soft spike in distribution in terms of size. They all fall within 100 and 5000 nanometers (0.1 and 5 microns), except for the steel fiber-reinforced concrete, whose particles are smaller than the other mixes. After that, regular, fly ash, then slag is the progression for overall largest of the fine particles. This suggests that although adding classically fine particles like fly ash and slag cause more aerosol particles to form, the resulting particles are typically larger when compared to the few very small particles generated by adding macroscale steel fibers. It may be hypothesized that the potential to participate in the hydration reaction allows the finer admixtures to bind and stiffen the cement matrix evenly, while the larger inert macroscale admixture acts as a composite and introduces stress concentrations within the cement to encourage local crushing and the generation of nanoscale particles.

4.5 Mechanical Properties

The following mechanical properties are computed from the load data. The ultimate strength and Young's modulus are taken to be actual values, even if they do not match average values in the field. The linear elastic fracture energy observed is a global value, and is used in conjunction with comminution theory.

The ultimate strength is taken from the peaks of the load curves for each concrete, and averaged among specimens of the same concrete. The Young's modulus is taken as the slope from a linear regression of the data where the load is linear with displacement. The observed linear elastic fracture energy comes from the integral of the load-displacement data, with the complimentary energy subtracted from this (even though it is not much), as explained in Section 2.6.1.

Table 4: Mechanical Properties Observed for each Concrete Tested

Concrete Type	**Average Ultimate Strength (ksi)**	**Average Young's Modulus (ksi)**	**Average Observed Linear Elastic Fracture Energy (J)**
Regular	3.61	565	197
Slag	5.17	738	279
Fly Ash	6.17	773	375
Wire-Reinforced	3.78	570	295

As expected, the wire-reinforced did not affect compressive strength. However, fly ash and slag contributed significantly to the strength of the mix. Likewise, the wire-reinforced concrete was just as stiff as the regular concrete, but slag and fly ash both added significant stiffness as well. However, the observed LEFM energy was raised by similar magnitudes with all inclusions, small and large alike.

Looking at the statistics of the data itself, it is evident that some spreads are large (high standard deviation and variance), and/or lopsided (high |mean-median|), but the trends are still there. A one-way analysis of variance (ANOVA) analysis yields distinct groups of points, and the probability of a null correlation is essentially zero for all three variables. See Section 4.6 for the statistics of the data and the results of the ANOVA analysis.

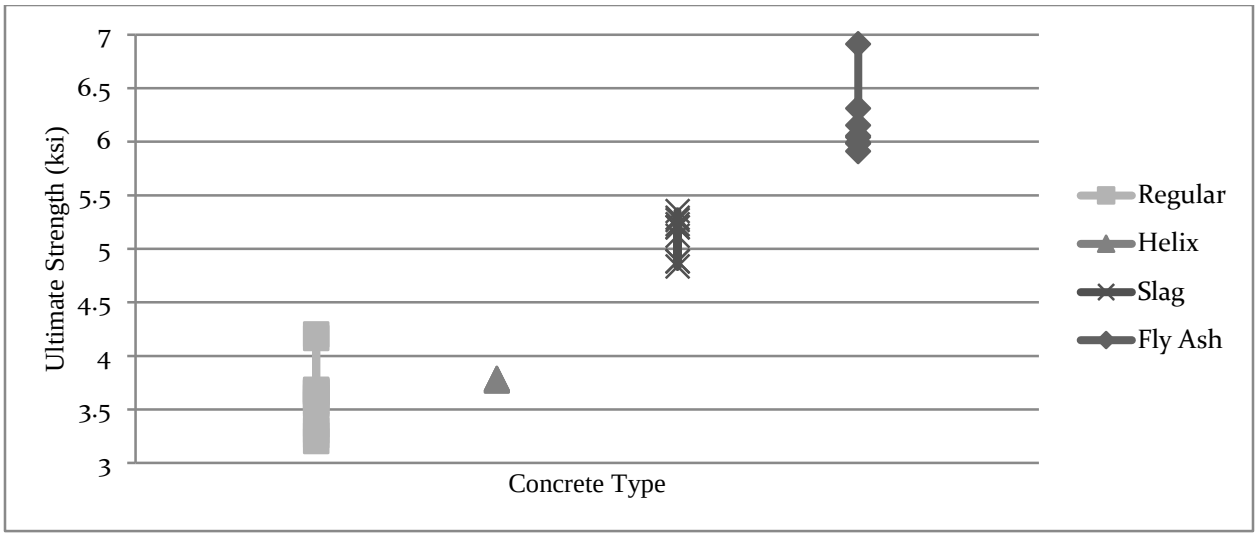

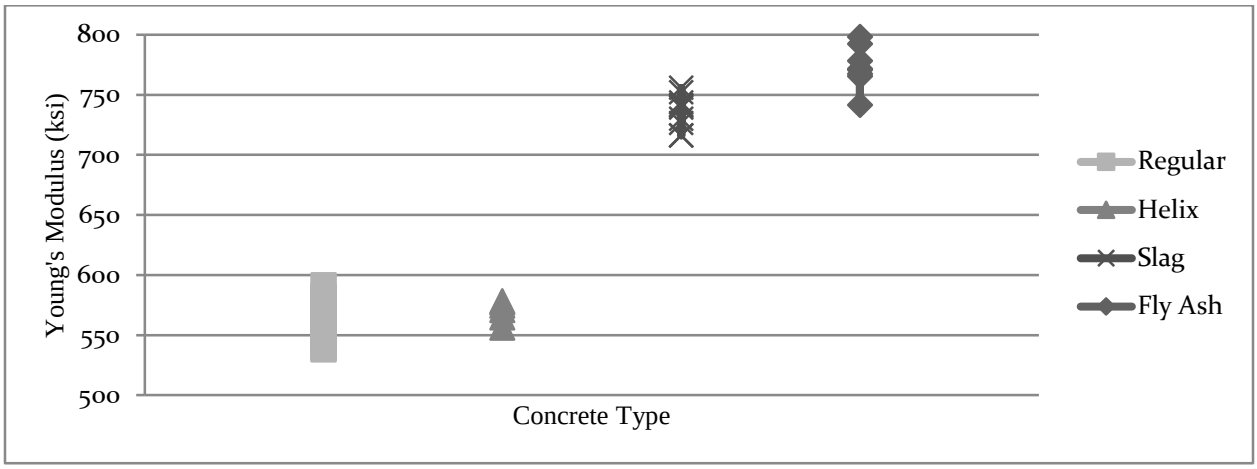

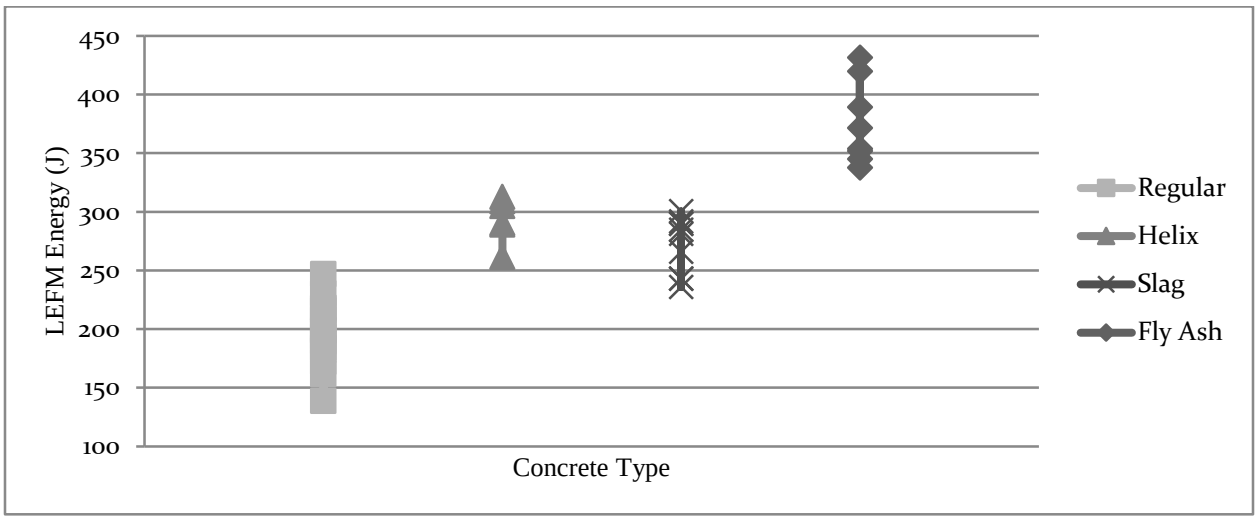

Figure 22a, (First), Figure 22b (Second), Figure 22c (Third)

The data spreads for each mechanical property show good rends despite some large scatter.

4.6 Statistical Properties

The statistical properties presented for this data are the standard deviation, the variance, and the difference between median and mean for each type of concrete. In addition, the spreads were analyzed together, with a one-way analytical variance (ANOVA) computation.

Table 5: Statistical Measurements for Mechanical Properties

Concrete Type	Ultimate Strength (ksi)			Young's Modulus (ksi)			Observed Linear Elastic Fracture Energy (J)		
	Std. Dev.	Var.	|Mean-Median|	Std. Dev.	Var.	|Mean-Median|	Std. Dev.	Var.	|Mean-Median|
Regular	0.284	0.080	0.006	16.8	283	3.58	27.6	762	1.03
Slag	0.176	0.031	0.047	12.0	144	2.37	23.1	535	8.51
Fly Ash	0.324	0.105	0.121	17.4	303	1.95	35.2	1242	12.4
Steel Fiber	0.008	0.000	0.001	8.5	71.9	2.36	18.9	357	2.99

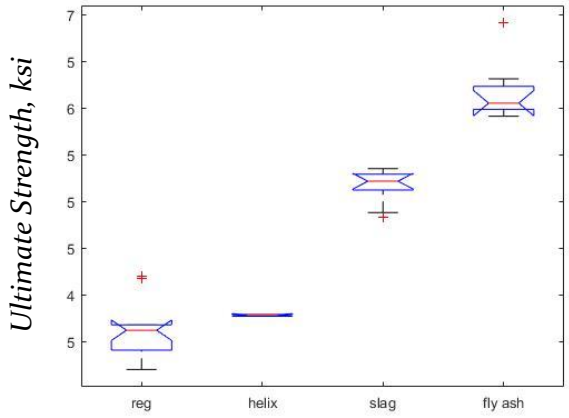

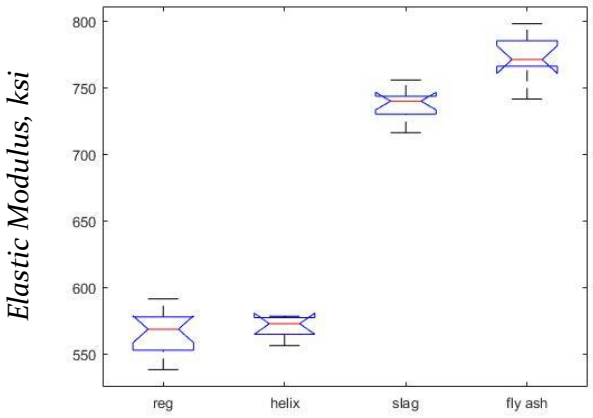

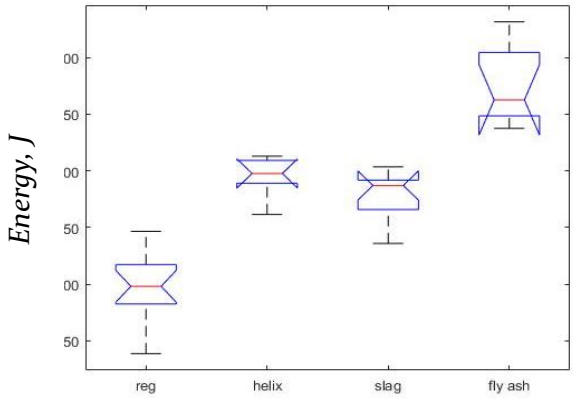

Concrete Type	Number of Trials
Regular	15
Steel Fiber	6
Slag	10
Fly Ash	8

Figure 23a (Top Left), Figure 23b (Top Right), Figure 23c (Bottom Left)

The ANOVA analysis further illustrates clear trending despite some large data spreads.

5 NUMERICAL MODELING

A finite element model was performed in ABAQUS to simulate the stress redistribution from stiffer inclusions. The basic two-dimensional model tests whether there is a stress concentration in the concrete at the tips of a steel fiber under a dynamic wave of stress applied over 0.1 second. Then, a variance of the aspect ratio of the stiffer inclusion tests whether a smaller aspect ratio reduces that stress concentration.

There is one steel fiber with dimensions from this thesis, and 3”x3” of concrete. For simplicity, with recognition of the inaccuracy, the concrete is a homogeneous perfectly elastic material with a Poisson’s ratio of 0.22, and a Young’s modulus of 550 ksi, matching the regular concrete from the experiments. For dynamic loading, its structural damping ratio is taken as 0.02, and its density is assumed to be 145 pci, so its mass density is entered as 65.8 kg/ci. The steel is a solid strip approximating the wound steel fiber. Its Poisson’s ratio is 0.3, its Young’s modulus is 29000 ksi, its structural damping ratio is 0.05, and its mass density is 228 kg/ci. A perfect bond is assumed and programmed with merging the two instances. A linear stress is applied at the top for 0.1 second, with roller-pin boundary conditions restraining the other three edges.

In the model, it was found that there does exist a stress concentration when a stress wave passes through the stiff inclusion (See Figure 24). It is true that according to the wave speed of concrete, the front and the back of the stress wave should be a distance that is hundreds, if not thousands of times larger than the height of the experimental specimens. However, it is also true that stiffer material attracts load, and, similarly, stiffer material conducts stress propagation faster, which also leads to stress concentration. This is supported by steel’s larger wave speed than that of concrete. In an analysis of steel in mechanical systems, the wave speed was cited as 5140

meters per second[44], while an analysis of concrete piles gave a common range of 3000-4500 meters per second[45].

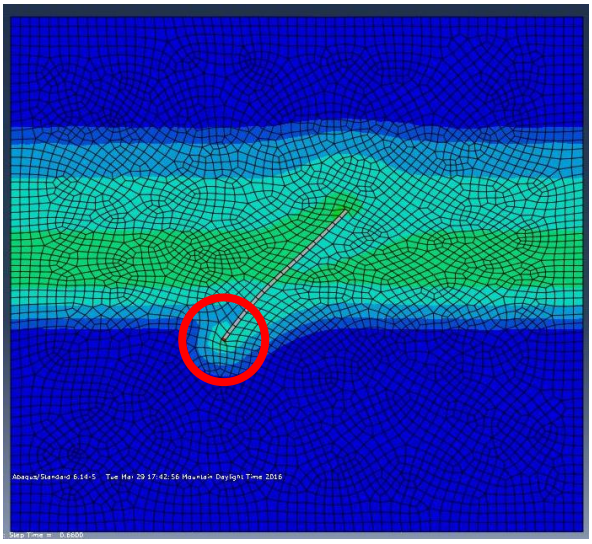

Figure 24

This finite element model predicts that a stress wave is focused into the points of the surrounding material adjacent to the ends of a stiffer fiber, modeled as steel in concrete

In addition to concentrating it, the stiffer element attracts and channels the stress, only making these concentrations more definite. It was also found that the less the aspect ratio, the less the concentrated stress (See Figure 25).

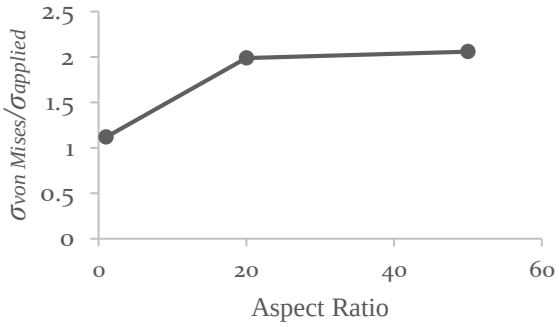

Figure 25

The aspect ratio of the stiff fibrous inclusion considered in concrete tends to decrease the stress concentration at either end of the fiber.

[44] Hussein, 2
[45] Moradi, 232

The concentrated stress is measured as the maximum stress seen in either element adjacent to each end of the fiber. This shows that theoretically, stiffer inclusions that are longer concentrate more stress. The fracture pattern for this concrete under crushing stress can be predicted with the stress contours, following them perpendicularly (See Figure 26).

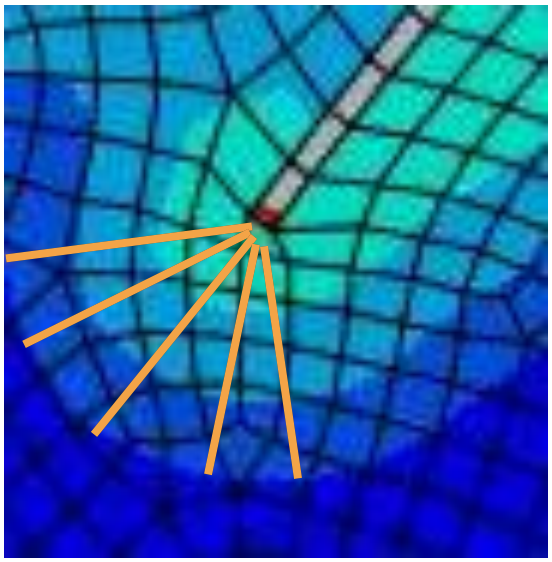

Figure 26

It is likely that radial microcracks form perpendicular to the stress contours, creating smaller aerosol particles than the other mixes. More testing is required to confirm this.

6 ANALYSIS

6.1 Comparison to Theoretical Results

By integrating established theories with this empirical work, a verification of the assumptions that lead to predictions of the mechanical behavior can be attained. Three theories are applied: linear elastic fracture mechanics (LEFM), comminution, and fragmentation. Of the several statistics-based fragmentation theories that exist for brittle materials, Gilvarry's theory was used for this thesis. If the comminution energy is consistent with what the mining industry sees with similar ore, even after a correction of the LEFM energy, then the fracture behavior assumed through comminution theory is confirmed to occur in these concrete mixes. If the size

distribution that was measured matches Gilvarry's predicted distribution for fragmentation, then that theory applies well to these cases. However, if nothing can be confirmed, then these predictions of mechanical behavior are inconclusive, and more tests are required.

6.1.1 Linear Elastic Fracture Mechanics Comparison

It was found that the theoretical error for the aggregate used is predicted to be 20-25%. This difference in aggregate size should be eliminated in future. However, the current data can be used to produce energy values that are theoretically "corrected." (See Appendix IV: Calculations, See Table 6 for the values.) This deviation could potentially explain any discrepancies involving the energy of comminution.

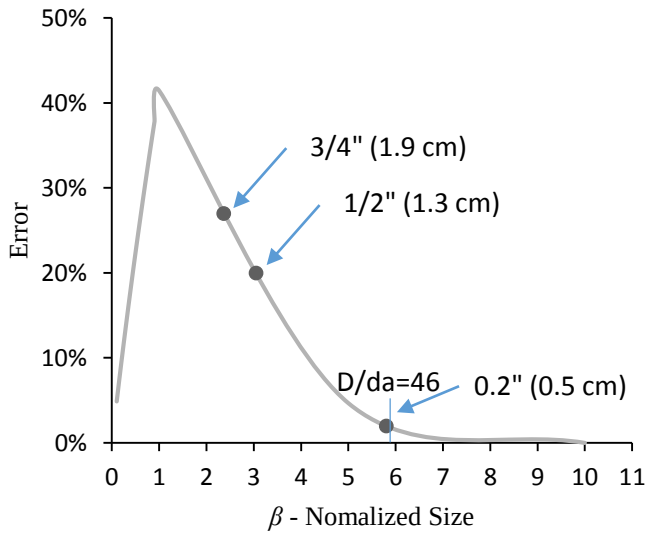

Figure 27

The LEFM Error is computed as the difference in true strength (See Appendix IV), and the assymptotes it approaches on either side. Only three cylinders were cast with gravel sieved so that D/da was 46.

Table 6: Corrected Energy Values

Concrete Type	Average Observed Linear Elastic Fracture Energy (J)	Corrected Value According to Size Effect (J)
Regular	197	155
Slag	279	220
Fly Ash	375	295
Wire-Reinforced	295	246

6.1.2 Comminution Comparison

It is difficult to apply the original comminution theory directly to this application due to the multiple scales of fracture. If it is applied to a distribution of particle sizes, then mathematically, the energy required to comminute the particles from one size down to the next increases exponentially, which does not make sense. If it is assumed that all the comminution energy goes to creating the large pieces, then the Bond Work Index can be calculated from the energy computed. Rearranging Equation 9, Equation 15 is produced.

$$W_i = \frac{0.1E}{\left[\frac{1}{\sqrt{x_2}} - \frac{1}{\sqrt{x_1}}\right]}$$

Equation 15

Using 6 inches (150000 microns) as an average particle size representing the specimen, and breaking them to 3 inches (75000 microns), which is about what was measured for the primary fracture debris, combining these sizes with the energy measured for each concrete yields the Bond Work Index for each concrete.

Table 7: Bond Work Index Computed for each Concrete

Concrete Type	Using Non-Corrected Energy (kWh/short ton)	Using Corrected Energy (kWh/short ton)
Regular	1.22	0.956
Slag	1.78	1.40
Fly Ash	2.39	1.86
Wire-Reinforced	1.76	1.46

These values are far lower than the 10-20 kWh per short ton for limestone ore, and they only decrease when Equation 15 is applied to smaller particle sizes. This could be explained by the stiffness and strength being below average, but this seems low for a material like this. Limestone has a similar compressive strength and fracture toughness to concrete.

6.1.3 Fragmentation Comparison

According to Gilvarry, the distribution of fragment sizes from single brittle fracture can be predicted if the spatial distribution of flaws is known. The distribution of all macro-scale particles (>150 microns) is shown for fly ash and slag, due to the fact that this was only done when the load curves were redone. Using Gilvarry's mathematical derivation, a single flaw density per volume can be translated to the parameters that go into the exponent, the ones valid for larger fragments (See Appendix IV: Calculations).

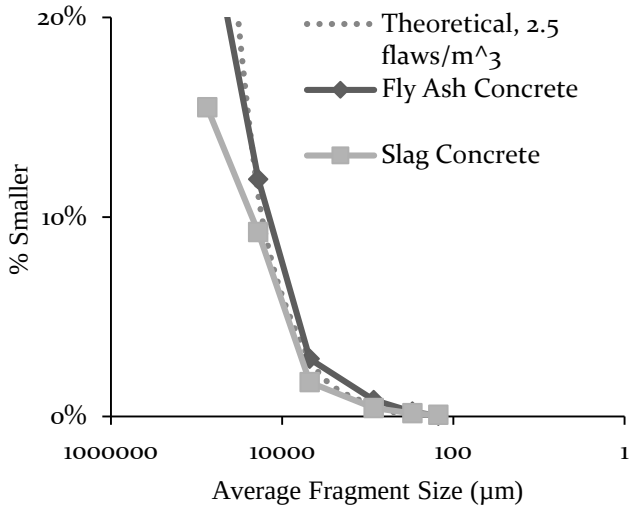

Figure 28

The size distribution of macro-scale fragments for slag and fly ash concretes shows that more of the concrete mass tends to fracture into larger pieces. The curves follow an exponential distribution well, but the parameter to achieve a good fit means a very low flaw density.

In order to fit the theoretical curve anywhere close to the empirical curves, the flaw distribution needs to be enormously small (2.5 per cubic meter). This could mean Gilvarry's theory does not apply well in this case, as concrete is a non-homogeneous, quasi-brittle material that could potentially not be subjected to single brittle fracture in this experiment (due to the imprecise time at which loading terminates). Gilvarry validates his theory with hardened gelatin samples, something much more homogeneous and brittle. If the theory does not apply well, then more of the concrete mass tends to fracture into larger pieces, with secondary debris crumbling off these fracture surfaces. At smaller scales, Gilvarry's theory simplifies to an exponential equation with the average edge-flaw spacing as the sole parameter controlling the distribution[30], which is a more reasonable value at 1.64 cm. However, fitting an exponential curve to the size data from SEM imaging of the fly ash and slag concrete is difficult due to a drop-off in size distribution at the microscopic level (See Figure 29).

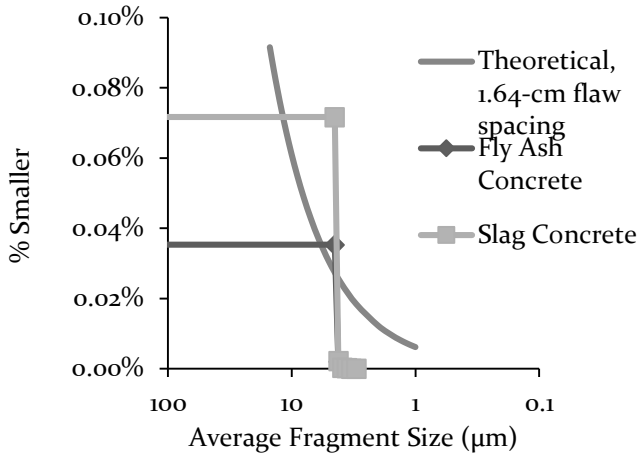

Figure 29

The size distribution of micro-scale fragments for slag and fly ash concretes shows that there is one specific size of aerosol that was observed from both mix. Due to this, these curves do not follow an exponential RRSB distribution very well. In addition, the parameter to achieve the best fit means a very high flaw spacing.

This could mean an adjusted fragmentation theory is required. Specifically, Gilvarry's theory may be adapted to consider inclusions embedded in concrete. From numerically modeling a stress wave propagating through concrete with a steel fiber, it is known that there is a stress concentration at the ends of the fibers as the wave passes through the fiber. It is suspected that the smaller particles collected from the fiber-reinforced concrete are from these stress concentration points. If this is the case, then there is a subdomain of micro-flaws ready to produce these particles, distributed about the tiny zone adjacent to each fiber endpoint.

$$P_{micro}(n_{micro}|t_{micro}) = \frac{e^{-\gamma_{micro}t_{micro}}(\gamma_{micro}t_{micro})^{n_{micro}}}{n_{micro}!}$$

Equation 15

Assuming this is independent of the macro-flaw distribution (which it physically cannot be), then the same derivation for the distribution applies:

$$Y(x) = 1 - e^{\frac{x}{k_{micro}}}$$

Equation 16

However, unity of the smaller particles approximately equals the total volume of the small zones adjacent to each fiber endpoint. So Equation 16 becomes:

$$Y(x) = \frac{V_{fiber\ ends}}{V_{total}} - e^{\frac{x}{k_{micro}}}$$

Equation 16

Where *V* represents volume. It makes sense to take the volume at the end of a fiber as the portion of the volume affected by the stress concentration. With the right *k* values, superimposing the two distributions should give a flattened lump in the finer particle region (See Figure 30), which is more representative of the precise size range of aerosols that were sampled.

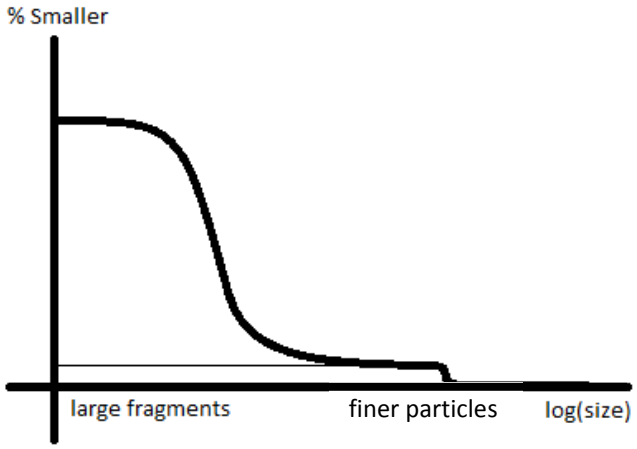

Figure 30

Gilvarry's theory can be adjusted to include a superimposed distribution of fine particles, which tends to be a certain size.

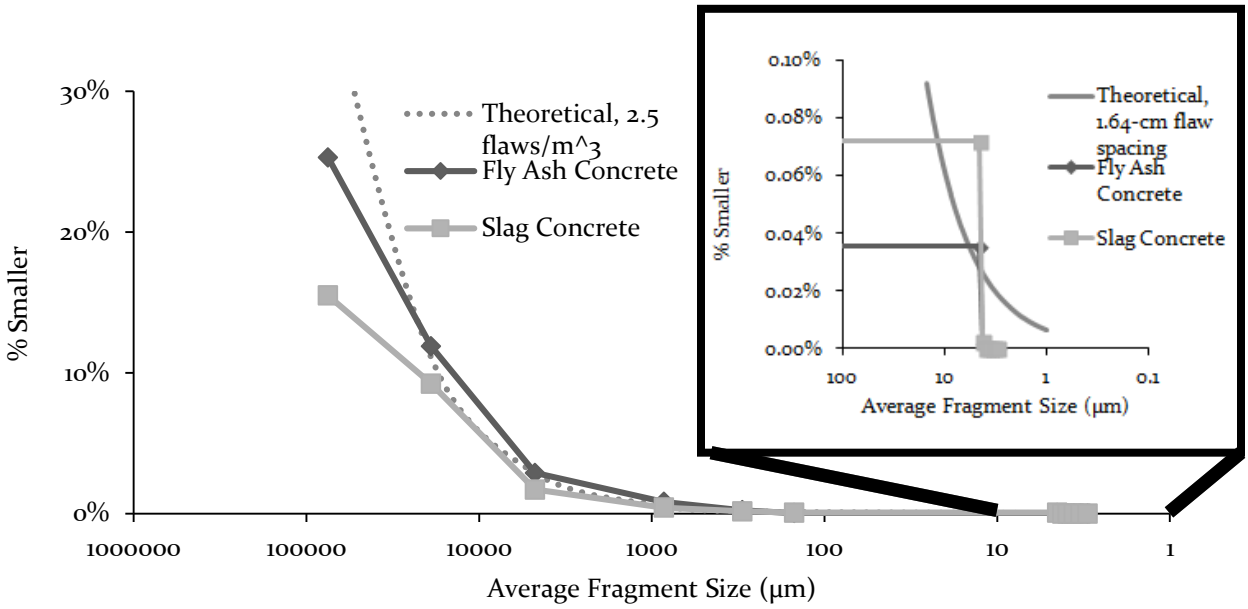

Figure 31

For comparison, the entire distribution is shown. A jump is observed at fine particles approximately 5 microns large.

7 CONCLUSIONS

Recall, the questions addressed were:

(a) How do inclusions to the mixture such as slag, fly ash, and steel fiber reinforcement, affect the concentration of airborne particles during failure?

(b) What particle characteristics, such as size distribution, shape, and quantity result from these inclusions?

(c) Is there a difference in mechanism between particle production with macro-scale inclusions, such as steel fiber reinforcement, and micro-scale inclusions, such as fly ash and slag?

It has been shown in this thesis that the scale and type of inclusion significantly affects not only concrete properties, but the size of particles produced when shattered. This difference is pronounced differently in the characterization of the macro-scale fragments, and the aerosol particles collected from the air. For example, the slag concrete held together better than the fly ash concrete, producing more primary large fragments, as exemplified by the higher percent smaller at that size (See Figure 28). Another example, at the micro-scale, is that the steel fiber-reinforced concrete was able to produce smaller particles than any other mix.

The particle characteristics were found for the four mixes. It was found that in terms of both mass of particles collected, and airborne concentration, the fly ash concrete produced the most, then the slag concrete, then the regular concrete, then the steel fiber-reinforced concrete. A totally different trend exists for the airborne particle sizes: the slag concrete produced the largest overall, then the fly ash concrete, then the regular, then the steel-fiber at the smallest. For shape factors, preliminary imaging shows that elongation of particles exists.

After comparing empirical data to existing theories by applying them, it is clear that there is a need to develop extensions to account fracture of heterogeneous material with inclusions. If successful, more could be known about the mechanisms through which these particles are produced. Based on this thesis, it may be concluded that steel fibers cause the concrete to produce smaller particles, despite these inclusions being much larger than the fly ash and slag, so there is a difference in mechanism for production of the particles.

As stated previously, for the hypothesis to be plausible, the following criteria must be satisfied:

(a) Microscopic concrete particles produced from microfracture must be small enough to become airborne and interact with human lung tissue.
(b) These particles must be elongated enough to be prone to lodging in lung tissue or cause inflammation.
(c) There must be large enough concentrations of these particles in the air in order for there to be an increased likelihood of inhalation of these particles.
(d) The mix itself must be brittle enough to be capable of producing such particles.

Firstly, the microscopic particles that form can clearly become airborne. Due to the violent nature of the loading, the energy released during fracture is great and sudden. This allows dust to go flying off the sample. This was recorded by the DustTrak initially, and there was enough sampled from the air to take measurements as well.

Secondly, these particles show evidence of having elongated shapes. The SEM images illustrate shape factors greater than the health threshold. However, the implication of causing inflammation in lung tissue and harm to the lung cells is not confirmed until a full inflammation

and toxicity analysis can be conducted. In preliminary tests, a marker for toxicity was found in the smaller distribution of particles from the concrete with steel fibers, and all particle samples showed repulsive zeta potentials, essentially meaning they will not clump together, which can be a problem when interacting with lung tissue.

Thirdly, the concentrations produced by continuously loading these concrete mixes to failure greatly exceed clean and healthy values. Even the lower concentration produced by the steel-fiber reinforcement is high enough to exceed the more rigorous European standard. It is clear that clouds of concrete dust can accumulate if a disastrous event has ensued on a concrete structure.

Finally, the mixes have all shown to be fully capable of producing PM10 aerosols. Despite the difficulties in successfully applying theories behind this behavior, it is evident what can be produced from which type of inclusion, and it can be deduced why the characteristics of these particles are different between each inclusion. It is suspected that stress concentrations from the presence of the steel fibers plays a role in the fragmentation of the concrete around them, setting it apart from the other mixes.

The basic hypothesis that more PM10 airborne particles are produced from inclusions such as fly ash, slag, and steel fiber-reinforcement, is valid for only the micro-scale inclusions, but the particles that are produced from including steel fibers may be more harmful, according to the toxicity marker in the distribution of the particles it produced. The prediction that these particles show signs of being harmful is inconclusive at this point. They can definitely be inhaled, and can interact with lung tissue, but the effects on long-term health from that interaction requires more testing.

8 FUTURE WORK

Future work to be done to continue this work should include crushing of more concrete specimens, enough to yield a sufficient amount of particles for toxicity analysis. In addition to fly ash, slag, and steel fibers, inclusions like silica fume and nano-particles may be tested. All particles should be collected and sieved for completeness of the fragment size distribution, and specimens must be capped with sulfur in order to obtain reasonable energy data. Enough aerosol particles should be sampled for a full toxicity test, both in-vitro and in-vivo. Additionally, Gilvarry's theory may be adapted to consider the viscoelastic effects within the concrete matrix to account for the time dependent quasi-brittle response of the concrete microstructure to an applied stress wave. This stress wave should also be applied to a numerical model with a material more representative of concrete in order to confirm the phenomenon of stress concentration at the ends of the steel fibers when subjected to such a stress wave.

REFERENCES

AASHTO Standard M295, 2011, “Specification for Coal Fly Ash and Raw or Calcined Natural Pozzolan for Use in Concrete.”

“A fast method for simulating destruction and the generated dust and debris.” *The Visual Computer*: 65-67, 111.

ASTM Standard C33, 2013, "Specification for Concrete Aggregates," ASTM International, West Conshohocken, PA, 2013. DOI: 10.1520/C0033_C0033M-13. www.astm.org

ASTM Standard C150, 2005, "Specification for Portland Cement," ASTM International, West Conshohocken, PA, 2005. DOI: 10.1520/C0150-05. www.astm.org

ASTM Standard C618, 2015, "Specification for Coal Fly Ash and Raw or Calcined Natural Pozzolan for Use in Concrete." ASTM International, West Conshohocken, PA, 2015. DOI: 10.1520/C0618-15.

Bažant, Zdeněk, et al. “What did and did not cause collapse of World Trade Center Twin Towers in New York?” *Journal of Engineering Mechanics* (2008): 900, 905.

Bažant, Zneděk, Jaime Planas. *Fracture Size Effect in Concrete and Other Quasibrittle Materials.* CRC (1998): 9, 30, 111.

Bažant, Z. P., Y. W. Kwon. “Failure of slender and stocky reinforced concrete columns: tests of size effect.” *Materials and Structures* 27 (1994): 87

Cooke, W. E. “Fibrosis of the lungs due to the inhalation of asbestos dust.” *British Medical Journal* 2 3317 (1924): 147.

Forquin, P., Erzar, B. “Dynamic fragmentation process in concrete under impact and spalling tests.” *International Journal of Fracture* 163 1 (2010): 193-215.

Gilvarry, J. J. “Fracture of solids I: distribution function for fragment size in single fracture (theoretical).” *Journal of Applied Physics* (1961): 392-9.

Griffith, A. A., “The phenomena of rupture and flow in solids.” *Philosophical Transactions of the Royal Society of London* A221 (1921): 163-98.

Hering, Susanne. V. “Impactors, Cyclones, and Other Particle Collectors.” In *Air Sampling Instruments for Evaluation of Atmospheric Contaminants.* ACGIH, Cincinnati (2001): 280.

Hill, Jason S., et al. “Performance characterization of MiniVol PM2.5 sampler. *92nd Annual Meeting of the Air and Waste Management Association* (1999): 9.

Hussein, Mohamad, Michael Morgano. “Structural Integrity Evaluation of Concrete Piles from Stress Wave Measurements.” *Society for Experimental Mechanics Conference on Nondestructive Testing of Concrete in the Infrastructure* (1993): 2

Irwin, G. “Analysis of stresses and strains near the end of a crack transversing a plate,” *Journal of Applied Mechanics* 24 (1957): 361-4.

Kosmatka, Stephen H., Michelle L. Wilson. *Design and Control of Concrete Mixtures*. Portland Cement Association, Skokie (2011): 49, 51, 59, 69-70.

Landrigan, Philip J., et al. “Health and environmental consequences of the World Trade Center disaster.” *Environmental Health Perspectives* 112.6 (2004): 731.

Martel. “Thermodynamics of fracture growth.” Lecture, University of Hawaii. 9.

McGee, John K., et al. “Chemical analysis of World Trade Center fine particulate matter for use in toxicological assessment.” *Environmental Health Perspectives* 111.7 (2003): 972.

MiniVol TAS Operation Manual Rev. 1.2. Airmetrics: 10, 17, 28.

Momber, Andreas. “The fragmentation of standard concrete cylinders under compression: the role of secondary fracture debris.” *Engineering Fracture Mechanics* 67 (2000): 445-59.

Moradi, Rasoul, et al. “Impact Analysis of Mechanical Systems Using Stress Wave Propagation Methodology.” *AcademyPublish.org*: 232.

Neville, A.M. *Properties of Concrete*. John & Wiley Sons, Inc., New York (1996): 16-17, 36, 414.

Oberdörster, Günter, et al. “Nanotoxicology: an emerging discipline evolving from studies of ultrafine particles.” *Environmental Health Perspectives* 113.7 (2005): 827.

Rabczuk, T., Eibl, J. “Simulation of high velocity concrete fragmentation using SPH/MLSPH.” *Numerical Methods in Engineering* 56 10 (2003): 1421-1444.

Tanaka, Tatsuo. “Comminution laws: several probabilities.” *Industrial & Engineering Chemistry Process Design & Development* (1966): 353.

Thompson R. J., A. T. Visser. “Benchmarking and management of fugitive dust emissions from surface mine hauls.” *Institution of Mining and Metallurgy* Trans A (2002): 111.

Uenishi, Koji, et al. “Dynamic fragmentation of concrete using electric impulses.” *Construction and Building Materials* 67B (2014): 170-179.

APPENDIX I: PROCEDURE FOR PRODUCTION AND COLLECTION OF AIRBORNE COMMINUTED CONCRETE PARTICLES

Research Focus

This procedure focuses on the question of how fractures propagate and forms particles under rapid overloads. Preliminary testing shows aspect ratio and spatial distribution can statistically quantify fracture growth at all scales.

Thesis Hypothesis

Based on preliminary results showing that spatial distribution and aspect ratio are critical properties that determine fracture growth and the particles it produces, it must be possible that particle size, shape and distribution can be predicted through these quantities, along with fracture energy. It is imperative that several different types of concrete are crushed to test this hypothesis. Regular, slag, fly ash, and Helix-reinforced concrete are crushed, and their airborne particles collected.

Procedure Overview

In this procedure, an MTS machine crushes concrete in direct compression, at a rate rapid enough to produce airborne dust. The dust is then collected onto a filter by a machine called a Mini Vol. The filter is later analyzed for the particles it collected. For reference, a DustTrak also estimates the particles in the air optically, and records them in real time.

This procedure tests concrete in compression, so standard cylinders must be cast and cured. This process follows a process compliant with ASTM Standard C192/C192M, Standard Practice for Making and Curing Concrete Test Specimens in the Laboratory. Another process required for preparation of testing is the specific cleaning standard followed for the collection equipment, which involves several lab chemicals. Once the equipment is cleaned, and the concrete is cured, the specimens can be broken out of their molds and set up for testing, along with the Mini Vol, DustTrak, and the rest of the setup, which involves a form of isolation. Testing the concrete cylinders in compression follows procedures observed in the laboratory hosting the MTS machine, which should be compliant with ASTM C39/C39M, Standard Test Method for Compressive Strength of Cylindrical Concrete Specimens. Once the tests are completed, some fragments are kept or photographed for reference, the filters holding the particles are labeled and put in cold storage, and the area is cleaned up.

Materials and Equipment

Materials:

- Concrete Ingredients
- Additives
- Water
- Sulfur Capping Compound
- Chemical Cleaning Agents (Isopropynol, Hexane, Dichloromethane)

Equipment:

- Standard Mixing Equipment (Trowel, Rod, Utility Knife, Wheelbarrow)
- Electric Mixer
- 4” diameter by 8” tall cylindrical forms
- Curing Room
- Sulfur Crockpot and Ladle
- 4" Capping Apparatus
- MTS Materials Testing Machine
- Standard MTS Maintenance Tools
- DustTrak
- Mini-Vols
- Pre-Weighed (Untreated) Filters
- Gilibrator
- Standard Chemical Lab Equipment (Kim Wipes, Teflon Gloves, Lab Grease, Tweezers, Scrub Brush)
- Camera
- Painter's Tarp
- Duct Tape
- Storage Buckets

Procedure

Specimen Preparation

The preparation of the specimens includes mixing, pouring, curing, and capping. The content of water, cement, and aggregate follows the amounts recommended on the ready-mix package. The mixing process adheres to the following procedure, which is compliant with ASTM Standard C192/C192M:

- Rinse the electric mixer.
- According to the desired mix design and volume, measure the appropriate weights of dry ingredients of cement, gravel[i], sand, and additive (if chemical), and pour into mixer.
- Run the mixer for one minute, and ensure that the dry components are nearly homogenous, then add a weight of water desired for the mix.
- Run the mixer for three minutes.
- Rest the mixture for three minutes.
- Run the mixer for another two minutes.
- Pour out the mixture, and place it into 4”x8” plastic cylindrical forms using trowels, three layers at a time, following methods laid out in ASTM C192 7.3.2.
- After each layer, consolidate the wet concrete using rods, following the methods laid out in ASTM C192 7.4.2.
- Store the cylinders in the curing room, which should be maintained around 30 centigrade and 100% relative humidity, for 28 days.
- Cap the specimens for even distribution of force[ii], following methods laid out in ASTM C617, Standard Practice for Capping Cylindrical Concrete Specimens. Use the designated crockpot to

melt the sulfur compound chips (at about 300 degrees Fahrenheit), under a fume hood, then scoop about a half-ladle at a time into the capping apparatus. Immediately take the specimen and carefully slide it down the guide, keeping it flush with it in order to keep it as close to perpendicular as possible, and into the molten liquid, holding it there for 20-30 seconds while the compound cools, and forms the bearing surface for loading.

Apparatus Setup

Because dust collection is involved, the MTS machine should be isolated from ambient conditions. A tarp slung over the machine is the simplest method (See Figure 1). A better method is a constructed chamber (See Figure 2). In this case, the safety enclosure was utilized as a sealed chamber, with painter's tarp and duct tape.

Figure I: Testing Isolation- Tarp

Figure II: Testing Isolation- Chamber

Set up the Mini Vol and DustTrak machines so that their sensor/inlet is about level with the bottom of the cylinder, and several inches away from the edge of the cylinder (See Figure 2). The closest ASTM standards that apply to dust sampling are ASTM D7201-06, Standard Practice for Sampling and Counting Airborne Fibers, Including Asbestos Fibers, in the Workplace, by Phase Contrast Microscopy, and ASTM F50-12, Standard Practice for Continuous Sizing and Counting of Airborne Particles in Dust-Controlled Areas and Clean Rooms Using Instruments Capable of Detecting Single Sub-Micrometre and Larger Particles.

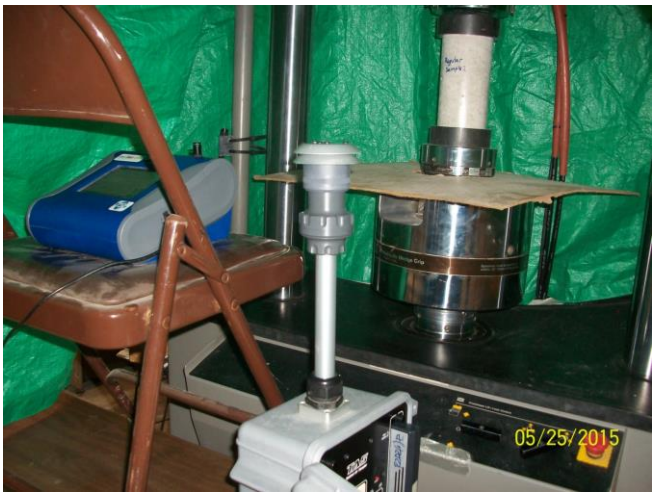

Figure III: Collection Setup- Tarp Enclosure

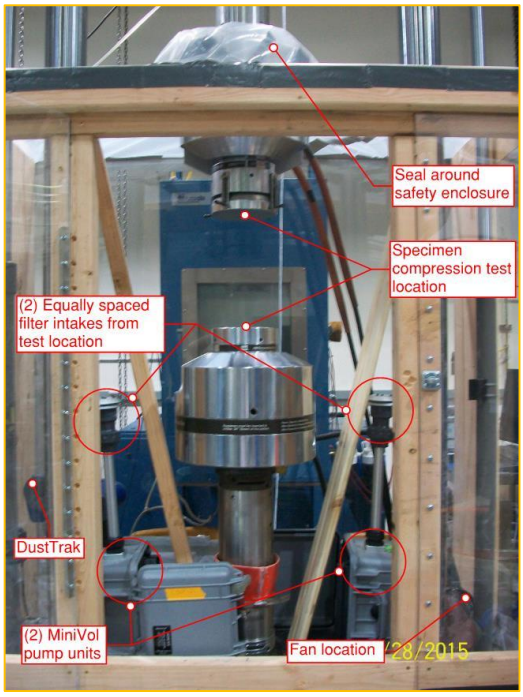

Figure IV: Collection Setup- Chamber Enclosure

Before the Mini Vol can be used, however, its components must be cleaned following laboratory cleaning protocol. The procedure for setting up and running the machines is as follows:

- Clean all components to each Mini-Vol apparatus with a half-hour soap bath, a thorough rinse with distilled water, a thorough rinse with isopropynol, and for the metal components, continue with a thorough rinse with hexane under a fume hood, and a thorough rinse with dichloromethane under a fume hood.
- Wrap all components in baked aluminum foil for sterile storage.

- Calibrate the flow in the Mini-Vol using a Gilibrator. The ideal flow given the ambient conditions can be calculated using guidelines laid out by the manufacturer.
- Assemble the components of the apparatus on a Kim wipe while wearing Teflon gloves, placing a pre-weighed filter in the filter assembly with Teflon tweezers rinsed with isopropynol (see Figure 5).

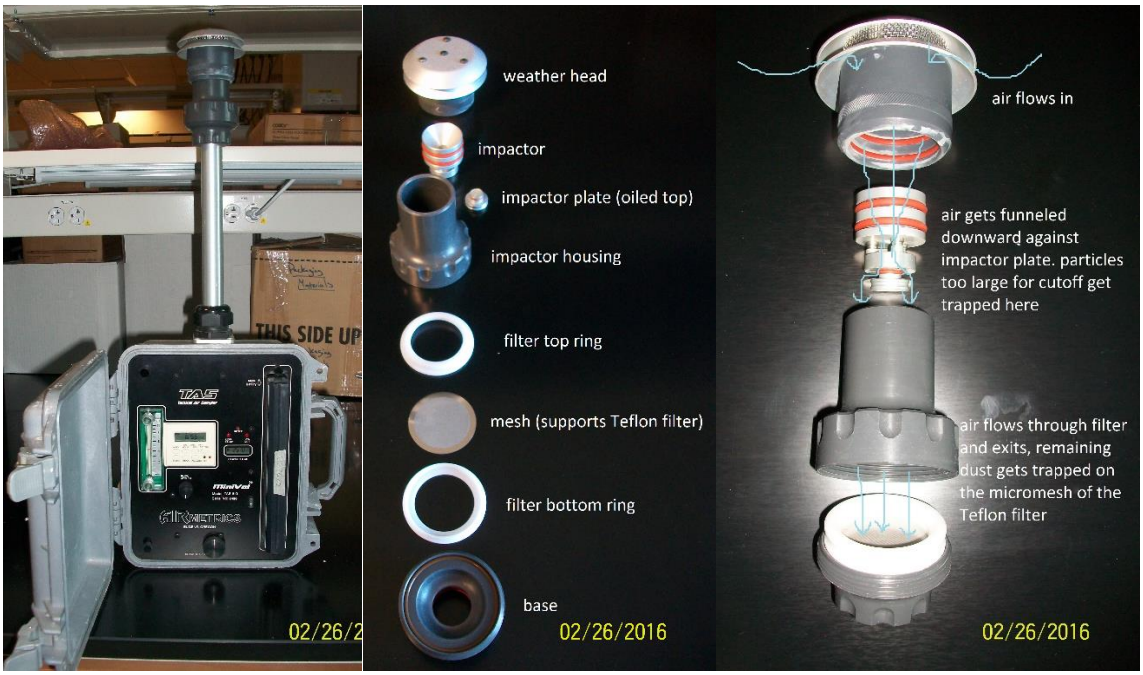

Figure V: MiniVol Filter Assembly (PM 2.5)

- Place the assembly on the machine that has been set up.
- Program the Dust Trak to sample for an appropriate amount of time.
- Plug in and set into place the Dust Trak.

Crushing and Collection

Start-up, calibration, and preparation for the tests follow requirements given by the manufacturer of the machine and the procedures of the laboratory. The stress-strain relations should be recorded for available reference. The procedure for loading these samples complies with ASTM C39/C39M:

- Start up the machine and its companion software.
- Place a piece of cardboard that can catch falling debris around the bottom platen. If debris is desired to be kept for later analysis, it is recommended that more cardboard is set up to entrap it in one area (See Figure 6).

Figure VI: Setup of Sampling Equipment

- Load the capped specimen on the bottom platen of the machine.
- Raise the bottom platen so that the top cap of the sample touches the loading platen.
- Apply a small load so that the test can run without any movement.
- Ensure the Mini Vols and DustTrak are running, and the environment is sealed.
- Begin loading at a rapid rate.
- Immediately after the first failure, which at high load rates, will be a near-instantaneous fracture, spalling, fragmentation, or comminution, stop loading.
- Wait fifteen minutes so that any airborne debris can be adequately sampled by the Mini Vols.
- Pick up any large pieces before placing the next specimen, and repeating the process for all specimens.

Cleanup

- Shut down MTS machine, following the appropriate protocol.
- Turn off the DustTrak, ensuring the data has been saved.
- Turn off the Mini Vols and disassemble their components, removing the filters and placing them in the Petri dishes they came from with Teflon tweezers.
- Close the dish, noting which way is up, and then wrap the closed dish with Teflon tape.
- Keep the petri dishes in cold storage.
- Put aside the rest of the components, as they need to be cleaned for reuse.
- Photograph or collect any fragments of the specimens desired and either discard the pieces in appropriate concrete disposal, or keep them for record.
- Clean the rest of the debris around the machine and take down the setup.

SEM Imaging

The filters can be imaged under a scanning electron microscope (SEM), observing procedures laid out in ASTM E766-14. The basic procedure includes the following steps:

- Carefully remove sampled filters with Teflon gloves and Teflon tweezers, and place on the plate that fits in the holding tray of the SEM.
- Gently tape the edges of the filter down to the plate.
- Place the sample in the tray, close the chamber, and evacuate the chamber.
- Use the SEM's companion software, to navigate the sample at the microscopic level to look for particles.
- Save images of a large sample size of particles, ensuring the scale is on the image for later measuring of the particles.
- Refill the chamber with air so that the sample can be removed.
- Carefully place the sample back into the petri dish with Teflon gloves and Teflon tweezers rinsed in isopropynol, and return to cold storage.

Data Processing

The data collected from this test includes the following:

- Particle sample
- Airborne particle concentration records
- Force-displacement curves
- Images of the macro-fractures observed
- SEM Images of the particles collected on the filters

This data from the MTS machine and the DustTrak can be processed immediately after testing. By integrating the force-displacement curve, the fracture energy can be estimated. The DustTrak records concentrations of dust it sees over time. This amount of dust in the air can be multiplied by the Mini Vol's flow rate and the time elapsed to provide a rough estimate of the mass of the dust particles collected on the filter. Until the filter is weighed, this is the only way to get an idea of what was collected. The images can be graphically processed for size and shape, and that data can be plotted and analyzed for statistical purposes.

[i] It should be noted that normal gravel has been shown to cause a distortion known as the size effect whenever measuring fracture parameters in concrete. According to Zdenek Bazant, who discovered this phenomena, in order for this distortion to be under 2% error, the maximum aggregate size should be less than or equal to the depth of the specimen over 46. This is approximately 0.2 inches, which is only possible to guarantee by sieving.

[ii] It is highly recommended not to test without sulfur capping. There is a method to place metal caps with rubber inserts. However, this is advised against because when fracture energy is of interest, it is inaccurately measured with the soft rubber absorbing so much of that energy.

APPENDIX II: FURTHER INFORMATION ON MIX COMPONENTS

TABLE 1 Grading Requirements for Fine Aggregate

Sieve (Specification E11)	Percent Passing
9.5-mm ($^3/_8$-in.)	100
4.75-mm (No. 4)	95 to 100
2.36-mm (No. 8)	80 to 100
1.18-mm (No. 16)	50 to 85
600-µm (No. 30)	25 to 60
300-µm (No. 50)	5 to 30
150-µm (No. 100)	0 to 10
75-µm (No. 200)	0 to 3.0[A,B]

(A) For concrete not subject to abrasion, the limit for material finer than the 75-µm (No. 200) sieve shall be 5.0 % maximum.

(B) For manufactured fine aggregate, if the material finer than the 75-µm (No. 200) sieve consists of dust of fracture, essentially free of clay or shale, this limit shall be 5.0 % maximum for concrete subject to abrasion, and 7.0 % maximum for concrete not subject to abrasion.

4.2.4.4 The appropriate limit for coal and lignite (see Table 2). If not stated, the 1.0 % limit shall apply,

[34]

TABLE 3 Grading Requirements for Coarse Aggregates

Size Number	Nominal Size (Sieves with Square Openings)	Amounts Finer than Each Laboratory Sieve (Square-Openings), Mass Percent													
		100 mm (4 in.)	90 mm ($3^1/_2$ in.)	75 mm (3 in.)	63 mm ($2^1/_2$ in.)	50 mm (2 in.)	37.5 mm ($1^1/_2$ in.)	25.0 mm (1 in.)	19.0 mm ($^3/_4$ in.)	12.5 mm ($^1/_2$ in.)	9.5 mm ($^3/_8$ in.)	4.75 mm (No. 4)	2.36 mm (No. 8)	1.18 mm (No. 16)	300 µm (No. 50)
1	90 to 37.5 mm ($3^1/_2$ to $1^1/_2$ in.)	100	90 to 100	...	25 to 60	...	0 to 15	...	0 to 5	...	...	...	...	...	...
2	63 to 37.5 mm ($2^1/_2$ to $1^1/_2$ in.)	...	...	100	90 to 100	35 to 70	0 to 15	...	0 to 5	...	...	...	...	...	...
3	50 to 25.0 mm (2 to 1 in.)	...	...	...	100	90 to 100	35 to 70	0 to 15	...	0 to 5	...	...	...	...	...
357	50 to 4.75 mm (2 in. to No. 4)	...	...	...	100	95 to 100	...	35 to 70	...	10 to 30	...	0 to 5	...	...	...
4	37.5 to 19.0 mm ($1^1/_2$ to $^3/_4$ in.)	...	...	...	...	100	90 to 100	20 to 55	0 to 15	...	0 to 5	...	...	...	...
467	37.5 to 4.75 mm ($1^1/_2$ in. to No. 4)	...	...	...	...	100	95 to 100	...	35 to 70	...	10 to 30	0 to 5	...	...	...
5	25.0 to 12.5 mm (1 to $^1/_2$ in.)	...	...	...	...	...	100	90 to 100	20 to 55	0 to 10	0 to 5	...	...	...	...

[34]

contact lenses, if present and easy to do. Continue rinsing.
P308+P313 - If exposed or concerned: Get medical advice/attention.
P362 - Take off contaminated clothing and wash before reuse.
P403+P233+P405- Store in a well-ventilated place. Keep container tightly closed. Store locked up.
P501 - Dispose of contents/container in accordance with local, regional, national, territorial, provincial, and international regulations.

2.3. Other Hazards

Inhalation can cause serious, potentially irreversible lung/respiratory tract tissue damage due to chemical (caustic) burns, including third degree burns. Individuals with lung disease (e.g. bronchitis, emphysema, COPD, pulmonary disease) or sensitivity to hexavalent chromium can be aggravated by exposure. Heating the product or containers can cause thermal decomposition of the product and release hydrogen sulfide. Hydrogen sulfide is a highly flammable, explosive gas under certain conditions, is a toxic gas, and may be fatal. Gas can accumulate in the headspace of closed containers, use caution when opening sealed containers. The presence of heavy metals may cause sensitization in sensitive individuals. Risk of thermal burns on contact with molten product.

2.4. Unknown Acute Toxicity (GHS-US) No data available

SECTION 3: COMPOSITION/INFORMATION ON INGREDIENTS

3.1. Substances

Not applicable

3.2. Mixture

Name	Product Identifier	% (w/w)	Classification (GHS-US)
Slags, ferrous metal, blast furnace	(CAS No) 65996-69-2	100	Not classified
Contains	**Product Identifier**	**% (w/w)**	**Classification (GHS-US)**
Calcium oxide	(CAS No) 1305-78-8	30 - 50	Skin Irrit. 2, H315 Eye Dam. 1, H318 STOT SE 3, H335
Magnesium oxide (MgO)	(CAS No) 1309-48-4	> 0.1, 0.1 - 1, 1 - 5, 5 - 10, 10 - 20	Not classified
Quartz	(CAS No) 14808-60-7	< 1	Carc. 1A, H350 STOT SE 3, H335 STOT RE 1, H372

Slag is a nonmetallic byproduct from the production of iron. Trace amounts of chemicals may be detected during chemical analysis. For example, slag may contain trace amounts of manganese oxide, titanium oxide, chromium compounds, sulfur compounds, and other trace compounds.
Multiple WHMIS ranges have been utilized to account for varying concentration.
Full text of H-phrases: see section 16

SECTION 4: FIRST AID MEASURES

4.1. Description of First Aid Measures

General: Never give anything by mouth to an unconscious person. If you feel unwell, seek medical advice (show the label if possible).

Inhalation: When symptoms occur: go into open air and ventilate suspected area. Keep at rest and in a position comfortable for breathing. If you feel unwell, seek medical advice.

Skin Contact: Remove contaminated clothing. Gently wash with plenty of soap and water followed by rinsing with water for at least 15 minutes. Call a POISON CENTER or doctor/physician if you feel unwell. Wash contaminated clothing before reuse.

Eye Contact: Rinse cautiously with water for several minutes. Remove contact lenses, if present and easy to do. Continue rinsing for at least 60 minutes. Immediately call a POISON CENTER or doctor/physician.

Ingestion: Rinse mouth. Do not induce vomiting. Immediately call a POISON CENTER or doctor/physician.

4.2. Most Important Symptoms and Effects Both Acute and Delayed

General: Irritation to eyes, skin and respiratory tract. Causes serious eye damage.

[redacted]

REPORT OF FLY ASH ANALYSIS

Project Name: Laramie River
Sample ID #: 150604001
Sample Date: May 2015
Tested By: QC
Report Date: 10-Jul-15

CHEMICAL TESTS	RESULTS	ASTM C 618 CLASS F/C	AASHTO M 295 CLASS F/C
Silicon Dioxide (SiO_2), %	33.74		
Aluminum Oxide (Al_2O_3), %	17.96		
Iron Oxide (Fe_2O_3), %	5.93		
Sum of SiO_2, Al_2O_3, Fe_2O_3, %	57.63	70.0/50.0 min.	70.0/50.0 min.
Calcium Oxide (CaO), %	28.38		
Magnesium Oxide (MgO), %	6.18		
Sulfur Trioxide (SO_3), %	1.74	5.0 max.	5.0 max.
Sodium Oxide (Na_2O), %	1.80		
Potassium Oxide (K_2O), %	0.49		
Total Alkalies (as Na_2O), %	2.12		

PHYSICAL TESTS	RESULTS	ASTM C 618 CLASS F/C	AASHTO M 295 CLASS F/C
Moisture Content, %	0.02	3.0 max.	3.0 max.
Loss on Ignition, %	0.21	6.0 max.	5.0 max.
Amount Retained on No. 325 Sieve, %	15.30	34 max.	34 max.
Specific Gravity	2.73		
Autoclave Soundness, %	0.04	0.8 max.	0.8 max.
Strength Activity Index with Portland Cement at 7 days, % of Control	95.6	75 min.*	75 min.*
Strength Activity Index with Portland Cement at 28 days, % of Control	100.0	75 min.*	75 min.*
Water Required, % of Control	96.7	105 max.	105 max.
Loose Bulk Density, lbs/ft^3	76.9		

Meets ASTM C 618 and AASHTO M 295, Class C

*Meeting the 7 day or 28 day strength activity index will indicate specification compliance.

Melissa Garcia

Melissa Garcia
Quality Assurance / Laboratory Manager

APPENDIX III: COMPLETE DATA

All Load Curves

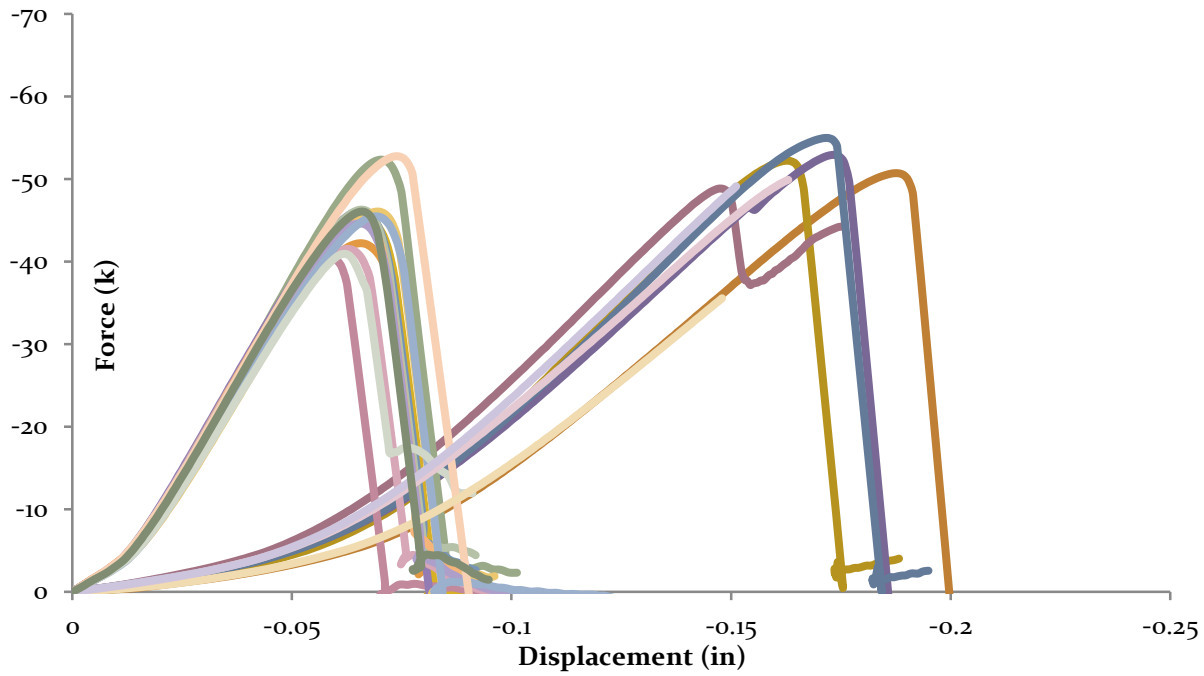

Load-Displacement Curves for Regular Concrete Specimens

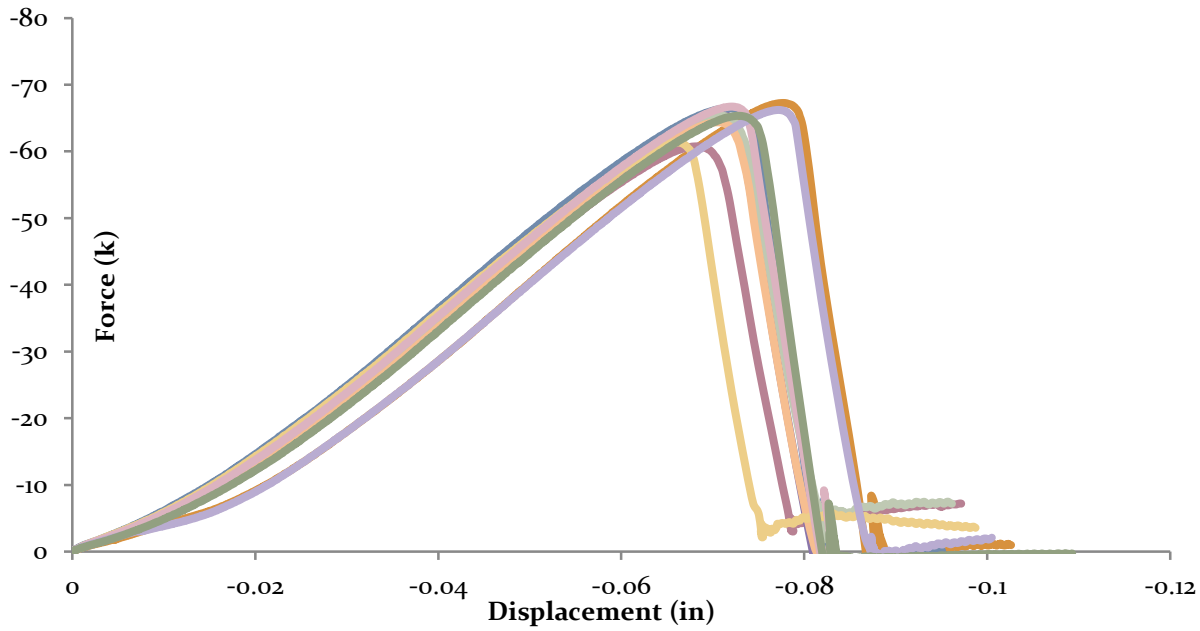

Load-Displacement Curves for Slag Concrete Specimens

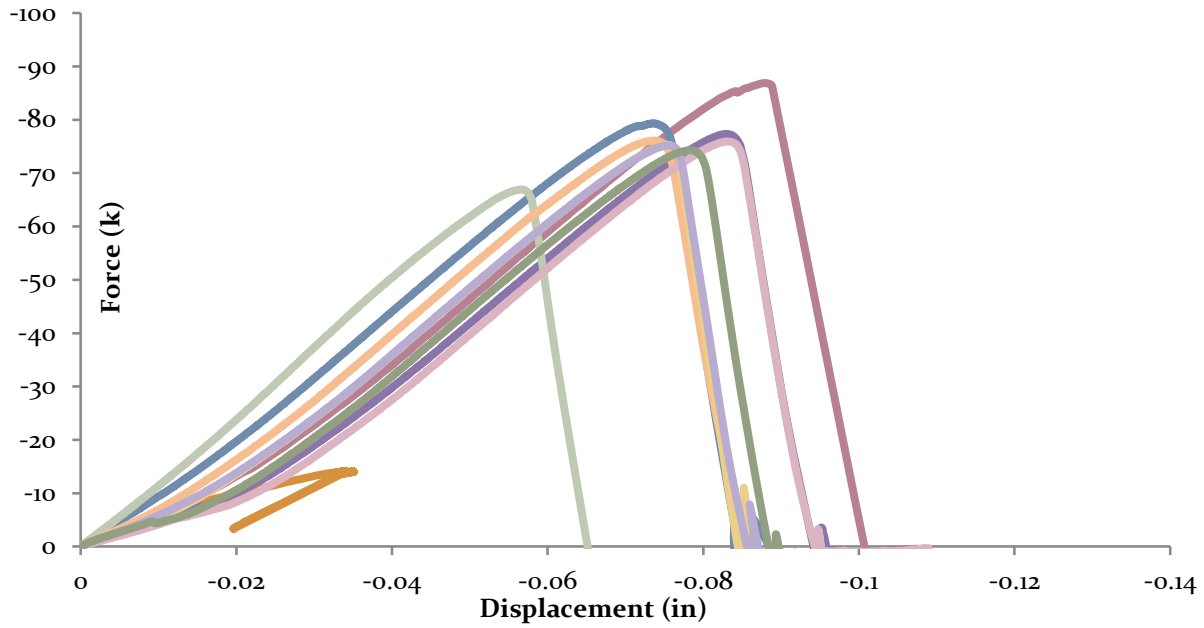

Load Displacement Curves for Fly Ash Concrete Specimens

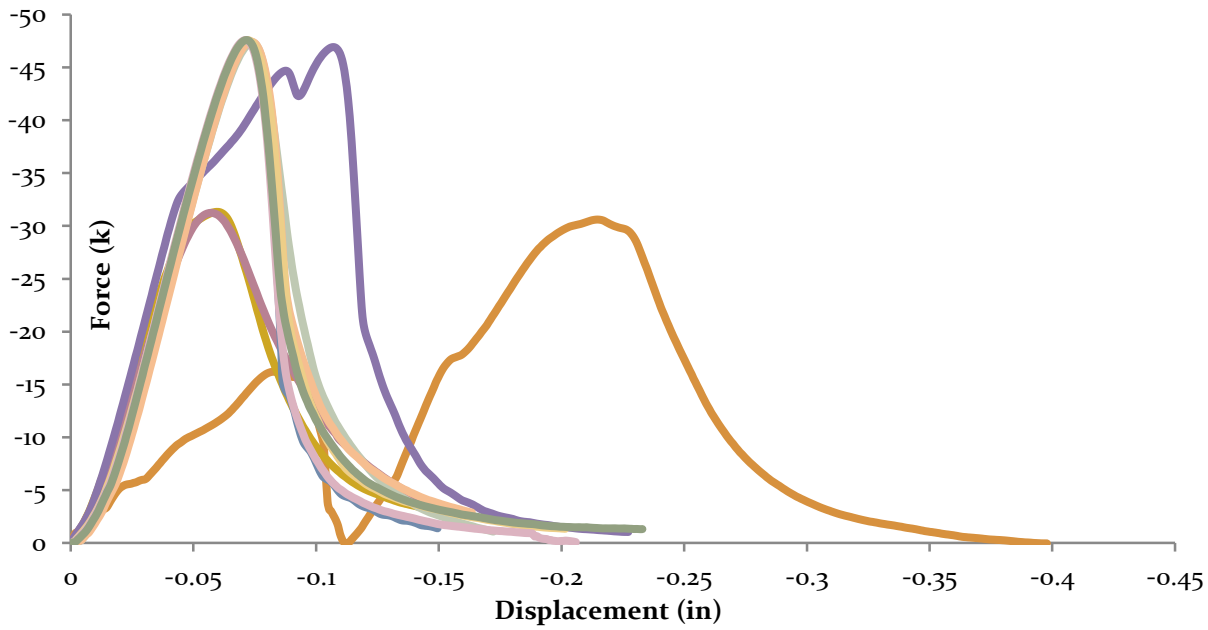

Load Displacement Data for Steel Fiber-Reinforced Concrete Specimens

Filter Mass Table (courtesy of Wyatt Champion, Lupita Montoya)

"Inputs"

Test Data			
Date	ID	Filter ID	
9/26/2015	Background	Eric 01	
	Helix Filter L	Eric 02	
	Helix Filter R	Eric 03	
	Regular Filter L	Eric 04	
	Regular Filter R	Eric 05	
	Slag Filter L	Eric 06	
	Slag Filter R	Eric 07	
	Fly Ash Filter L	Eric 08	
	Fly Ash Filter R	Eric 09	

All above pre weighs are from weigh date 9/23/15
All above post weighs are from weigh date 10/05/15

Copy and paste the section to the right, filter by filter, from the

Copied and Pasted from Gravimetric Entry Spreadsheets "Output" Tab

Type of Weight	Control Filter ID	Mass 1	Mass 2	Mass 3	Control Filter ID	Mass 1	Mass 2	Mass 3	Filter ID	Mass 1	Mass 2	Mass 3	Comments
		grams	grams	grams		grams	grams	grams		grams	grams	grams	
Pre	Control 1	0.16926	0.16933	0.16927	Control 2	0.17768	0.17762	0.17765	Eric 01	0.17227	0.1723	0	
Post	Control 1	0.16927	0.16926	0	Control 2	0.17764	0.17763	0	Eric 01	0.17232	0.1723	0	
Pre	Control 1	0.16926	0.16933	0.16927	Control 2	0.17768	0.17762	0.17765	Eric 02	0.17197	0.17198	0	
Post	Control 1	0.16927	0.16926	0	Control 2	0.17764	0.17763	0	Eric 02	0.172	0.17198	0	
Pre	Control 1	0.16926	0.16933	0.16927	Control 2	0.17768	0.17762	0.17765	Eric 03	0.17209	0.17208	0	
Post	Control 1	0.16927	0.16926	0	Control 2	0.17764	0.17763	0	Eric 03	0.17216	0.17215	0	
Pre	Control 1	0.16926	0.16933	0.16927	Control 2	0.17768	0.17762	0.17765	Eric 04	0.17303	0.17301	0	
Post	Control 1	0.16927	0.16926	0	Control 2	0.17764	0.17763	0	Eric 04	0.17354	0.1735	0.1735	Ripped
Pre	Control 1	0.16926	0.16933	0.16927	Control 2	0.17768	0.17762	0.17765	Eric 05	0.17114	0.17114	0	
Post	Control 1	0.16927	0.16926	0	Control 2	0.17764	0.17763	0	Eric 05	0.17171	0.1717	0	
Pre	Control 1	0.16926	0.16933	0.16927	Control 2	0.17768	0.17762	0.17765	Eric 06	0.16646	0.16647	0	
Post	Control 1	0.16927	0.16926	0	Control 2	0.17764	0.17763	0	Eric 06	0.16777	0.16776	0	
Pre	Control 1	0.16926	0.16933	0.16927	Control 2	0.17768	0.17762	0.17765	Eric 07	0.16547	0.16546	0	
Post	Control 1	0.16927	0.16926	0	Control 2	0.17764	0.17763	0	Eric 07	0.16655	0.16654	0	
Pre	Control 1	0.16926	0.16933	0.16927	Control 2	0.17768	0.17762	0.17765	Eric 08	0.16696	0.16695	0	
Post	Control 1	0.16927	0.16926	0	Control 2	0.17764	0.17763	0	Eric 08	0.16844	0.16841	0	
Pre	Control 1	0.16926	0.16933	0.16927	Control 2	0.17768	0.17762	0.17765	Eric 09	0.17147	0.17145	0	
Post	Control 1	0.16927	0.16926	0	Control 2	0.17764	0.17763	0	Eric 09	0.1736	0.17354	0.17353	Ripped

The section to the right is automated

Filter Mass				Control 1				Control 2			
Repeat Mass 1 needed for calc	Repeat Mass 2 needed for calc	Repeat Mass 3 needed for calc	Repeat Mass 1 needed for calc	Repeat Mass 1 needed for calc	Repeat Mass 2 needed for calc	Repeat Mass 3 needed for calc	Repeat Mass 1 needed for calc	Repeat Mass 1 needed for calc	Repeat Mass 2 needed for calc	Repeat Mass 3 needed for calc	Repeat Mass 1 needed for calc
0.17227	0.1723	0	0.17227	0.16926	0.16933	0.16927	0.16926	0.17768	0.17762	0.17765	0.17768
0.17232	0.1723	0	0.17232	0.16927	0.16926	0	0.16927	0.17764	0.17763	0	0.17764
0.17197	0.17198	0	0.17197	0.16926	0.16933	0.16927	0.16926	0.17768	0.17762	0.17765	0.17768
0.172	0.17198	0	0.172	0.16927	0.16926	0	0.16927	0.17764	0.17763	0	0.17764
0.17209	0.17208	0	0.17209	0.16926	0.16933	0.16927	0.16926	0.17768	0.17762	0.17765	0.17768
0.17216	0.17215	0	0.17216	0.16927	0.16926	0	0.16927	0.17764	0.17763	0	0.17764
0.17303	0.17301	0	0.17303	0.16926	0.16933	0.16927	0.16926	0.17768	0.17762	0.17765	0.17768
0.17354	0.1735	0.1735	0.17354	0.16927	0.16926	0	0.16927	0.17764	0.17763	0	0.17764
0.17114	0.17114	0	0.17114	0.16926	0.16933	0.16927	0.16926	0.17768	0.17762	0.17765	0.17768
0.17171	0.1717	0	0.17171	0.16927	0.16926	0	0.16927	0.17764	0.17763	0	0.17764
0.16646	0.16647	0	0.16646	0.16926	0.16933	0.16927	0.16926	0.17768	0.17762	0.17765	0.17768
0.16777	0.16776	0	0.16777	0.16927	0.16926	0	0.16927	0.17764	0.17763	0	0.17764
0.16547	0.16546	0	0.16547	0.16926	0.16933	0.16927	0.16926	0.17768	0.17762	0.17765	0.17768
0.16655	0.16654	0	0.16655	0.16927	0.16926	0	0.16927	0.17764	0.17763	0	0.17764
0.16696	0.16695	0	0.16696	0.16926	0.16933	0.16927	0.16926	0.17768	0.17762	0.17765	0.17768
0.16844	0.16841	0	0.16844	0.16927	0.16926	0	0.16927	0.17764	0.17763	0	0.17764
0.17147	0.17145	0	0.17147	0.16926	0.16933	0.16927	0.16926	0.17768	0.17762	0.17765	0.17768
0.1736	0.17354	0.17353	0.1736	0.16927	0.16926	0	0.16927	0.17764	0.17763	0	0.17764

Calculations - Filter samples		
Avg. Filter Pre	Avg. Filter Post	Difference
grams	*grams*	*grams*
0.172285	0.17231	0.000025
0.171975	0.17199	0.000015
0.172085	0.172155	0.000070
0.17302	0.1735	0.000480
0.17114	0.171705	0.000565
0.166465	0.167765	0.001300
0.165465	0.166545	0.001080
0.166955	0.168425	0.001470
0.17146	0.173535	0.002075

Calculations - Controls					
Avg. Control 1 Pre	Avg. Control 1 Post	Control 1 Difference	Avg. Control 2 Pre	Avg. Control 2 Post	Control 2 Difference
grams	*grams*	*grams*	*grams*	*grams*	*grams*
0.169265	0.169265	0.000000	0.177635	0.177635	0.000000
0.169265	0.169265	0.000000	0.177635	0.177635	0.000000
0.169265	0.169265	0.000000	0.177635	0.177635	0.000000
0.169265	0.169265	0.000000	0.177635	0.177635	0.000000
0.169265	0.169265	0.000000	0.177635	0.177635	0.000000
0.169265	0.169265	0.000000	0.177635	0.177635	0.000000
0.169265	0.169265	0.000000	0.177635	0.177635	0.000000
0.169265	0.169265	0.000000	0.177635	0.177635	0.000000
0.169265	0.169265	0.000000	0.177635	0.177635	0.000000

Calculations - Control differences			Calculations - Corrected masses		
Control 1 Difference	Control 2 Difference	Avg. Control Difference	Mass Collected	Mass Collected	Mass Collected
needed for calc	*needed for calc*	*grams*	*grams*	*grams (negative values = 0)*	*micrograms*
0.000000	0.000000	0.000000	0.000025	0.000025	**25**
0.000000	0.000000	0.000000	0.000015	0.000015	**15**
0.000000	0.000000	0.000000	0.000070	0.000070	**70**
0.000000	0.000000	0.000000	0.000480	0.000480	**480**
0.000000	0.000000	0.000000	0.000565	0.000565	**565**
0.000000	0.000000	0.000000	0.001300	0.001300	**1300**
0.000000	0.000000	0.000000	0.001080	0.001080	**1080**
0.000000	0.000000	0.000000	0.001470	0.001470	**1470**
0.000000	0.000000	0.000000	0.002075	0.002075	**2075**

Time Sampled	MiniVol Flow	Air Sampled	PM9.7 Conc	PM9.7 Conc	Corrected PM9.7 Conc	Corrected PM9.7 Mass
hours	*liters per minute (lpm)*	*liters*	*ug/m3*	*ug/m3*	*ug/m3*	*ug*
0.25	5.35	80	312		0	#DIV/0!
2.08	5.35	669	22	64	-289	-193
2.08	5.35	669	105		-207	-138
5.12	5.35	1642	292	318	-19	-32
5.12	5.35	1642	344		32	53
6.08	5.35	1953	666	609	354	692
6.08	5.35	1953	553		242	472
6.38	5.35	2049	717	865	406	832
6.38	5.35	2049	1013		701	1437

APPENDIX IV: CALCULATIONS

Linear Elastic Fracture Mechanics Error

The following equation by proposed by Bažant[46] is taken:

$$\sigma_N = Bf_t'\left(1+\frac{D}{D_o}\right)^{-\frac{1}{2}}$$

By taking B=1, and f't as 0.7√f'c (MPa), a term β is introduced as D/Do. The size effect curve is produced by varying β from 0.1 to 10.

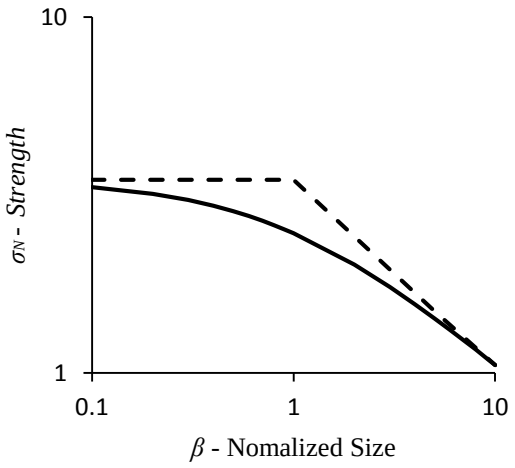

At β=1, there is an intersection of the horizontal and diagonal asymptotes. The diagonal portion is the prediction of strength using LEFM. The difference between these two curves is the error. At β~6, the 2% error limit occurs. Calibrating this as D/Do=46, given by Bažant for compression members, the error can be interpolated for with β=1 as an anchor, representing D/Do also equal to 1 (aggregate size the same size as the depth of the member). Because the strength is lower than predicted, the fracture energy must be lower than expected.

[46] Bazant, et al, 87

Comminution

Equation 9 is used for the Comminution Theory. W is found for the energy observed, which is converted from J/lb to kWh/short ton.

Fragmentation

Two measureable parameters of the concrete can be transformed into i, j, and k. This formulation is used for the larger pieces, and is assumed to be valid due to many similar shapes observed in the fragments. The two parameters are λ, the average density of Griffith flaws in the concrete volume, and L/w, the average shape factor for the simplified shape of fragments produced. The average size, x, is none other than:

$$x = \frac{L + w}{2}$$

L can be replaced with L and the shape factor, L/w:

$$x = \frac{w\left[\frac{L}{w}\right] + w}{2} = \frac{1 + \frac{L}{w}}{2} w \rightarrow w = \frac{2}{1 + \frac{L}{w}} x$$

Similarly, w can be replaced:

$$x = \frac{L + \frac{L}{\left[\frac{L}{w}\right]}}{2} = \frac{1 + \frac{w}{L}}{2} L \rightarrow L = \frac{2}{1 + \frac{w}{L}} x$$

This simplified shape is a cylinder, whereas Gilvarry requires edges to form. His shape is a three-sided polygon, so approximate L as *l*/3, or *l* =3L. So the linear characteristic ratio is:

$$\gamma_l = \frac{l}{x} = \frac{3L}{x} = \frac{6}{1 + \frac{w}{L}}$$

Similarly, the surface characteristic ratio is:

$$\gamma_s = \frac{s}{x^2} = \pi \mathrm{wL} = \frac{4\pi}{2 + \frac{L}{w} + \frac{w}{L}}$$

Finally, the volume characteristic ratio is:

$$\gamma_v = \frac{v}{x^3} = \frac{\pi \mathrm{Lw}^2}{4} = \frac{2\pi}{3 + \frac{w}{L} + \frac{3L}{w} + \frac{L^2}{w^2}}$$

Now the densities in each dimension shall be expressed through λ, through geometry of dimensions:

$$\lambda_v = \lambda, \lambda_s = \lambda^{\frac{2}{3}}, \lambda_l = \lambda^{\frac{1}{3}}$$

Finally, i, j, and k can be computed by combining the characteristic ratios and densities for each dimension:

$$i = \left(\frac{1}{\gamma_v \lambda_v}\right)^{1/3}, j = \left(\frac{1}{\gamma_s \lambda_s}\right)^{1/2}, k = \left(\frac{1}{\gamma_l \lambda_l}\right)$$

These quantities can be used to find Q from Equation 13, and ultimately, the theoretical distribution from the original two parameters.

Possible Earthquake Strain Rate

From ASCE 7-10:

- Base Shear, V=Sds*W/R
- Sds= ground acceleration
- W = weight of building

Example:

- Sds=1.473 g
- W=10,000 k (4-story heavy concrete)
- R=2
- V=7,365 k

Using Equivalent Force Method:

- 1,473 k on top floor, in one of the exterior frames

Potential Strain Rate:

- Assume 1'x2' beam: 1,473 k /(12"x24") = 5.11 ksi
- w/ 5 ksi concrete, strain is right around 0.003
- During Northridge Earthquake, maximum of 3.55 g/s of jerk was experienced
- 1.473 g/3.55 g/s = 0.415 s (time it takes to reach this load)
- 0.003/0.415 s = 0.007 s^-1

Lab Load Rate:

- 0.075 in/s
- 0.075 in/s /8 in = 0.009 s^-1